NTNU – Trondheim
Norwegian University of
Science and Technology

Ferromagnetic Resonance Spectroscopy Studies of Permalloy/Copper/Chromium/Copper thin films

Johannes Ofstad

Master of Science in Physics and Mathematics
Submission date: Januar 2014
Supervisor: Erik Wahlstrøm, IFY

Norwegian University of Science and Technology
Department of Physics

NTNU

Norwegian University of Science and Technology

Department of Physics

Master Thesis

Ferromagnetic Resonance Spectroscopy Studies of Permalloy/Copper/Chromium/Copper thin films

Author:
Johannes Ofstad

Supervisor:
Erik Wahlström

Foreword

This master thesis is the result of my work during the autumn semester 2013 and january 2014 at the Department of Physics, NTNU. My work has been carried under the supervision of Associate Professor Erik Wahlström. It is a continuation of the Specialization Project [1] which was done during the spring semester 2013.

It has been a long journey through the depths of condensed matter physics and experimental work. I've had the privilege to have the help and guidance of many kind people along the way. Whenever I needed guidance to get me in the right direction, or thoughtful input in my work, *Erik Wahlström* was never far away. I am thankful for your help, guidance, enthusiasm and motivation you've given me this past year. I am also thankful for the thoughts and inputs of *Vegard Flovik* (Erik's Ph.D student), which you provided during our meetings and at the lab. My work in this master thesis included fabrication of thin films at NTNU Nanolab. I would like to thank Nanolab engineer *Espen Rogstad* for giving me a lot of help in understanding the AJA sputter-instrument, which was used to create the thin films. He also helped fix the issues with the instrument, which hindered my work early on. Also, thank you Espen, for generously scribing each of my samples. You're work helped create very good samples. Since I was new at Nanolab and working alone, I would like to thank *Mark Chiappa* for giving me the introductory clean room course and initial training for the AJA Sputter. Ph.D student *Jonas Ribe* gave me a lot of generous help at the beginning of the lab work, in which I am thankful for.

Abstract

A theroretical and experimental study of 10Py/10Cu, 10Py/10Cu/xCr/10Cu (with x=4,7, 10,13 nm) thin films has been performed. The thin films were fabricated by the sputter deposition technique at NTNU Nanolab and afterwards a FMR-experiment were performed on them at the temperatures 180K, 210K, 240K, 280K, 330K and 360K. The anisotropy field, exchange bias and offset field were extracted and analysed. The results revealed vastly higher magnitude of anisotropy field and exchange bias for the 4 Cr film, compared to the other samples. Under 300K, the anisotropy field of 4Cr is ∼60 Oe which is about 30 times larger than anisotropy field of the other samples. The exchange bias for 4Cr is ∼8 Oe, which is about 10 times larger than the exchange bias of the other samples. The significant difference in exchange bias is explained by the spin-density wave amplitude, which increases for decreasing Cr-thicknesses. However, this model does not predict the large drop-off to the 7 Cr, 10 Cr and 13 Cr samples. The measurement of PyCu revealed an exchange bias of the same order as the 7-13 Cr samples, indicating that the exchange coupling between the Py and Cr layer is very weak, since it is of the same magnitude as the PyCu film. A theoretical description of H_{Res} and ΔH of the system was given, but not fulfilled. Factors, mainly due to spin pumping and interface effects must be identified and adapted to the equations.

Sammendrag

En teoretisk og eksperimentell studie av 10Py/10Cu, 10Py/10Cu/xCr/10Cu (med x=4,7, 10,13 nm) tynnfilm har blitt utført. Tynnfilmene ble laget med sputter deposisjon på NTNU Nanolab og etterpå studert med FMR-spektroskopi ved temperaturene 180K, 210K, 240K, 280K, 330K og 360K. Anisotropifeltet, exchange bias og offsett-feltet ble ekstrahert fra dataene og analysert. Resultatene viste en betraktelig høyere amplitude av anisotropi felt og exchange bias for 4 Cr-filmen, sammenlignet med de andre prøvene. Under 300K er anisotropifeltet for 4 Cr $\sim$60 Oe som er omtrent 30 ganger høyere enn de andre prøvene. Exchange biasen for 4 Cr er $\sim$8 Oe, som er omtrent 8 ganger høyere enn de andre prøvene. Den markante forskjellen er forklart med at spin-density-wave amplituden øker for mindre tykkelser av Cr. Men denne modellen forklarer ikke den markante reduseringen for de andre Cr-prøvene. Målingen av PyCu viste en exchange bias i samme størrelsesorden som 7-13 Cr-prøvene, noe som tilsier at exchange koblingen mellom Py og Cr-laget er veldig svak. En teoretisk beskrivelse av H_{Res} og ΔH ble gitt, men ikke fullført. Spin-pumping og interface-effekter må bli identifisert og tilpasset i modellene.

Contents

1 Introduction

Over the last 30 years, nano-scale structures has been extensively studied, as well as the development of experimental methods that allows us to explore their physical properties at this length scale. This is interesting for two reasons. First, new forms of matter with unique properties which is not found in naturally occurring materials can be fabricated. Second, the study of nanostructures open more possibilities for the development of very small devices. The giant magneto-resistance (GMR) effect (discovered in 1988) is an example of a scientific breakthrough which has impacted technology. GMR is a part of the scientific field *spintronics*, an emerging technology exploiting the intrinsic spin of the electron and its charge properties. Examples of spintronic-devices are modern hard drives, magnetoresistive random access memory (MRAM) and magnetic tunnel transistors (which has an advantage over conventional MOSFET devices).

The field of nanomagnetism has revealed that ferromagnetic thin-film structures, often incorporated into multilayer structures have dramatically different magnetic and transport properties than bulk magnetic matter. As an example [2], GMR of magnetic multilayers has been exploited to increase the capacity of hard discs by a factor of over 100 in a small number of years. New methods developed by scientists drive the field forward as more structures are studied.

The phenomenon of *exchange bias*, which is responsible for the shift of hysteresis loops along the H-axis, was discovered by Meiklejohn and Bean in 1956 [3]. Since that time, thousands of papers have been published on the topic. This extensive activity is principally due to the fact that virtually every computer containing a magnetic disc for information storage "reads" the stored bits with a device that utilizes exchange bias [2]. The technological application of exchange bias involves the interfacial magnetic exchange coupling of thin films of antiferromagnets (AFM) with ferromagnets (FM). Detailed information about the microstructure and magnetic states at the AFM/FM interface are required in order to model the exchange bias.

In this master thesis the aim is to further the understanding of the magnetodynamics, the spin-pumping, the effect of having an anti-ferromagnetic layer, chromium, along with a capping layer of copper, and a layer of copper in between the Permalloy and Chromium in FM/N/AFM/N thin-films. The films 10Py/10Cu, 10Py/10Cu/4Cr/10Cu, 10Py/10Cu/7Cr/10Cu, 10Py/10Cu/ 10Cr/10Cu, 10Py/10Cu/13Cr/10Cu that were used in the experiments were grown on 0.5 mm thick silicon wafers with 30 nm of SiO_2 on the surface. The thin film layers were created using the AJA Sputter at NTNU Nanolab. The experiments were performed by the ferromagnetic resonance technique, where the magnetodynamic properties were mapped.

Due to different antiferromagnetic/spin structuring, 4 different thicknesses of Cr are studied. Furthermore, temperature effects from 180-360K are also studied. In particular, the Néel temperature of bulk Cr is 311 K. Experiments will be performed to see if and how the system changes at this temperature. Afterwards, a summary and discussion of how each property varies with Cr-thickness and temperature will be presented.

The outline of this master thesis is as follows; section 2 reviews some relevant concepts of magnetism. Section 3 presents magnetic dynamics and ferromagnetic resonance. Section 4 presents antiferromagnetism and some examples of how it can be applied in thin films

and devices such as magnetic "read-heads" used in hard drives. Chromium and the spin-density-wave ordering is also presented. Section 5 describes spin-pumping, and how FMR is related to the topic. Subsequent sections describe spin propagation in thin film materials. The method, sputter deposition, used to create the thin films and the experimental method for both the film-fabrication and FMR-experiments is presented in section 6 and 7. Further on, the 5 thin film materials used in this project is presented in more detail in section 8. The results from the work is finally presented and discussed in section 9.

2 Magnetism

2.1 Diamagnetism and paramagnetism

All magnetic materials contain magnetic moments. The magnetic moment of a free atom has three principal sources: The electron spin, the orbital angular momentum about their nucleus and the change in the orbital momentum induced by an applied magnetic field. The *magnetization* $\vec{M}$ is defined as the magnetic moment per unit volume. The *magnetic susceptibility* per unit volume is defined as

$$\chi = \frac{\mu_0 M}{B} \tag{2.1}$$

where μ_0 is the vacuum permeability and B is the macroscopic magnetic field intensity. Materials with a negative susceptibility are called *diamagnetic* and materials with positive susceptibility are *paramagnetic*. In a paramagnet, the magnetic moments tend to be oriented randomly due to thermal fluctuations when there is no external magnetic field [4]. In an applied magnetic field these moments start to align parallel to the field such as the magnetization $\vec{M}$ of the material is proportional to the applied field. However, when the magnetic field is removed, the magnetization vanishes, as the magnetic moments within the material will orient randomly due to thermal motions. Paramagnetism is commonly found in atoms or molecules with an odd number of electrons. In general paramagnetic effects are quite small with magnetic susceptibility in the order of 10^{-3}-10^{-6} for most paramagnets [4]. The susceptibility of diamagnets are of the same order, meaning that the diamagnetic contribution is negligible in materials that show a form of ferromagnetism.

2.2 Ferromagnetism and magnetic energy

A ferromagnet has a spontaneous magnetization $\vec{M}$ even in the absence of an applied field. All the magnetic moments lie along a single unique direction. This effect is due to the domain structure of the ferromagnetic material. Only a few materials are ferromagnetic. The common ones are iron, nickel, cobalt and most of their alloys.

The free energy, crystalline structure and microscopic organization of a ferromagnet defines its magnetization dynamics. The main contributions to the magnetic free energy are exchange, Zeeman, magnetostatic and magnetocrystalline energy. Their typical values and dimensions are summarized in table 2.1.

Energy term	Dimension	Range
Exchange	[erg/m]	10^{-5} - $2 \cdot 10^{-4}$
Zeeman	[erg/m^3]	$\sim 10^9$ per Oe (for a 800 emu/cm^3 magnet)
Magnetostatic	[erg/m^3]	0 - $3 \cdot 10^{13}$
Magnetocrystalline	[erg/m^3]	$\pm(10^9$ - $2 \cdot 10^{14})$

Table 2.1: Overview of the various energies discussed in micromagnetism with typical magnitude ranges, after [5]

In the following section, each of the contributors will be presented.

2.3 Exchange energy

The exchange energy is a purely quantum mechanical effect, where neighbouring unpaired spins align, as determined by the Pauli exclusion principle and electric repulsion. In the

Heisenberg model, the exchange energy is given by

$$E_{\text{ex}} = -\frac{1}{2}\sum_{i<j} J_{ij}\vec{S}_i \cdot \vec{S}_j \tag{2.2}$$

where J_{ij} is the exchange integral, $\vec{S}_i$ and $\vec{S}_j$ are the nearest neighbour-spins. $J_{ij} > 0$ is a *ferromagnetic* order of the spins, while $J_{ij} < 0$ is an *antiferromagnetic* order. The spins are ordered in a positive or negative state as long as the system is below the Curie-Temperature T_C. Above T_C, the thermal energy surpasses the exchange energy and the spins will be unordered. The ordering is shown in figure 2.1 .

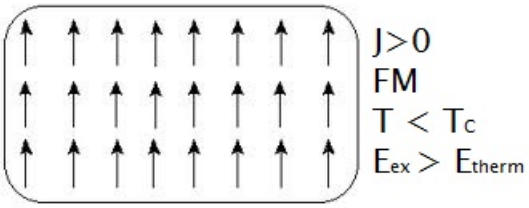

Figure 2.1: Illustration of ferromagnetic spin ordering.

2.4 Zeeman Energy

A ferromagnetic moment in an external magnetic field $\vec{H}_{ext}$ will have an energy related to its orientation in the field. In magnetics this is called the Zeeman energy, and the effect comes from exerting a torque on the magnetic moment. It is given by the integral

$$E_{\text{Zeeman}} = -\int_V \vec{H}_{ext} \cdot \vec{M}\mathrm{d}V \tag{2.3}$$

where $\vec{M}$ is the magnetization, and the integral is performed over the volume V of the stystem.

2.5 Magnetostatic self energy

The expression for the magnetostatic self energy is derived from Gauss' law of flux conservation

$$\nabla \cdot \vec{H} = -4\pi\nabla \cdot \vec{M} \tag{2.4}$$

At the surface, the magnetization is suddenly reduced to zero. According to equation (2.4), $\vec{M}$ has a non-zero divergence at the surface which causes an opposite divergence of $\vec{H}$. This field we name the demagnetization field $\vec{H}_D$. The energy associated to this field originates from (2.3) and is called the magnetostatic self energy

$$E_{\text{demag}} = -\frac{1}{2}\int_V \vec{H}_D \cdot \vec{M}\mathrm{d}V \tag{2.5}$$

Since the magnetic dipoles exists at the surface, it is evident that the geometry and the configuration of the magnetic specimen defines $\vec{H}_D$ and thereby E_{demag}. Equation (2.5)

also illustrates that E_{demag} depends on how the magnetization $\vec{M}$ is aligned on the object. The field dependence on geometry is normally given by the demagnetization tensor $\hat{N}$ such that $\vec{H}_D = -\hat{N} \cdot \vec{M}$.

The demagnitazation field $\vec{H}_D$ is very difficult to calculate even for the simplest case of uniform magnetization. But for a plane surface, with two of the axis infinite, $N_x = N_y = 0, N_z = 4\pi$. After conversion to standard spherical coordinates, the magnetostatic self energy becomes

$$E_{demag} = 2\pi M^2 \cos^2 \theta \tag{2.6}$$

(2.6) plane works really well for a thin film where the thickness t is much smaller than the lateral dimensions.

2.6 Magneto-crystalline anisotropy energy

Ferromagnets consists of small domains where the spins are aligned. But in separate domains, the spins point in different directions and their magnetic fields cancel out. Crystalline ferromagnets are normally anisotropic, meaning it takes more energy to magnetize the material in certain direction than others. The field strength required to reorient the magnetization vector differs with angle in respect to the crystal axis.

The primary source of magnetic anisotropy is the spin-orbit coupling [6]. The spin $\vec{S}$ is isotropic, while the orbital moments $\vec{L}$ are anisotropic. The magnetic anisotropy leads to a spontaneous positioning of the domains often referred to as the "easy" direction, indicating that this is the configuration which leads to the lowest energy. When a current or external field is applied, the configurations change to another state, referred to as the "hard" direction. The energy required to turn the magnetization away from the "easy" to the "hard" direction is given by the magnetocrystalline anisotropy energy.

The magnetocrystalline anisotropy energy is generally represented as an expansion in powers of the direction cosines of the magnetization. For a tetragonal system, using components $m_1 = M_x/\|\vec{M}\|$, $m_2 = M_y/\|\vec{M}\|$, $m_3 = M_z/\|\vec{M}\|$, and anisotropy constants K_i, we get

$$E_{\text{anis}} = K_2 m_3^2 + K_4 m_3^4 + K_{4'}(m_1^4 + m_2^4) + \cdots \tag{2.7}$$

in units per volume. Terms of order higher than 4 are usually neglected since their contributions are vanishingly small.

The magneto-crystalline parameters have a strong dependence on temperature [7]. They generally decrease rapidly than the magnetization as the temperature approaches the Curie temperature T_C.

2.7 Interfacial exchange energy

The exchange bias effect or exchange anisotropy arises from the interfacial exchange coupling between a ferromagnet and an antiferromagnet. Xi *et al* [8] modelled the interfacial exchange energy as a sum of the volume energy of the AFM-layer and the interfacial coupling energy:

$$E_{\text{interface}} = E_{\text{VolAFM}} - J_E \cos(\phi - \alpha) \tag{2.8}$$

E_{VolAFM} is an integral over the total volume of the antiferromagnet, where the exchange coupling constant, uniaxial anisotropy constant and the spatial orientation of the magnetic

moment structure is included. The moments at the interface of the ferromagnet and antiferromagnet are coupled together with the exchange coupling constant J_E. The interfacial exchange energy gives rise to an *exchange bias* field H_E, which will be presented in more detail in section 4.2.

2.8 Magnetic domains

A ferromagnet will depend on relevant energy terms and consist of multiple domains with different magnetization vectors. The domains are organized in such a way that the demagnetization energy is minimized. According to equation (2.5), this occurs when the number of surface poles are minimized. The orientation of the domains tend to lie towards the easy axis of the system, due to the influence of magnetocrystalline anisotropy.

Domain walls play a huge role in field-induced magnetization of ferromagnets. Here the mechanism is often nucleation and propagation of domain walls, sometimes hardened by structural and chemical inhomogeneities. When the small domains of the ferromagnet are easily migrated and thus magnetized at a low applied magnetic field, the material is a soft magnet. Soft magnets are easy to magnetize, and also easy to demagnetize. If a large magnetic field is required to migrate the domains and magnetize the material, the material is a hard magnet. It is more difficult to magnetize and demagnetize a hard magnet.

An effect known as *anisotropy dispersion* is due to inhomogeneities of the microscopic structure of the ferromagnet. This means a variation from place to place in the film, of the easy axis and/or the magnitude of the anisotropy constant. As a result, the direction of the local magnetization varies slightly from one point to another even within a domain.

2.9 Temperature dependence of the magnetization

The Curie temperature T_c is the temperature above which the spontaneous magnetization of a ferromagnet vanishes. Under T_c the parallel spin-alignment is held together exchange interactions (section 2.3). Kittel [9] postulates that exchange field $\vec{B}_e$ gives rise to the interactions, and is proportional to the magnetization $\vec{M}$, $\vec{B}_e = \lambda\vec{M}$ where λ is a constant independent of temperature. T_c can be found in terms of the mean field constant λ. This simplified model for $\vec{B}_e$ is called the *mean-field approximation*. In terms of the Curie constant C (a material-specific constant that relates the magnetic susceptibility to the temperature), λ can be determined

$$\lambda = \frac{T_c}{C} = \frac{3k_B T_c}{Ng^2 S(S+1)\mu_B^2} \tag{2.9}$$

where k_B is Boltzman's constant, g the gyromagnetic ratio, S the spin, μ_B the Bohr magneton and N the number of atoms per unit volume. The exchange field gives an approximate representation of the quantum mechanical exchange interaction.

The energy levels for an electron in an applied magnetic field B gives rise to energy level splitting. In a system with two energy levels, N_1 and N_2 are the electron population in each level. The resultant magnetization of N atoms per unit volume with magnetic moment μ is $M = N\mu \tanh(\mu B/k_B T)$. In the mean-field approximation (with the molecular field $B_e = \lambda M$ replacing the applied field B) below the Curie-temperature, the magnetization is

$$M = N\mu \tanh(\mu\lambda M/k_B T) \tag{2.10}$$

The curves of M as a function T obtained this way reproduce roughly the features of the experimental results , as shown in figure 2.2 for nickel. However, the mean field theory

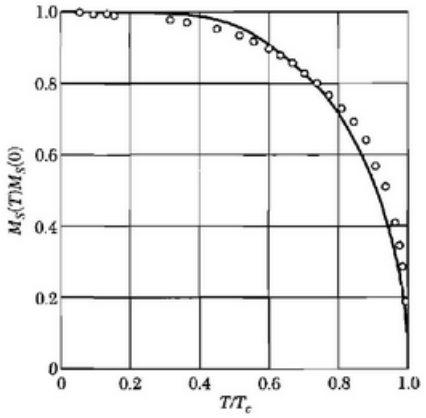

Figure 2.2: Saturation magnetization of nickel as a function of temperature, together with the theoretical curve for spin =1/2 on the mean field theory. Experimental values by Weiss and Forrer [10]. Figure is taken from [9].

doesn't give a good description of the variation of M at low temperatures. For $T \ll T_c$, the argument of tanh in equation (2.10) becomes large. The leading term of the magnetization deviation $\Delta M = M(0) - M(T)$ is from experiments found to have the form

$$\frac{\Delta M}{M(0)} = AT^{3/2} \tag{2.11}$$

Theoretically, well below the Curie temperature, this result can be explained in terms of thermal excitations of magnons [9]. This causes a decrease of spontaneous magnetization $M_s(T)$ and the result is the *Bloch* $T^{3/2}$ *law*:

$$M_s(T) = M_0(1 - bT^{3/2}) \tag{2.12}$$

where M_0 is the magnetization at zero temperature and the coefficient b is the Bloch constant depending on the spin-wave excitations of the system. The decrease of temperature enhances both the cubic anisotropy as well as the magnetization.

3 Ferromagnetic resonance

The ferromagnetic resonance (FMR) technique is among the most powerful experimental approaches to study the properties of ferromagnetic thin films. All essential magnetic properties can be extracted; magnetic anisotropies, Curie Temperature, gyromagnetic ratio, magnetic moment and relaxation mechanisms can be found with the right experimental setup [11] [12].

FMR arises from the precession of the (usually quite large) precession of the magnetization vector $\vec{M}$ inside a ferromagnet. The magnetization is stronger than paramagnets due to a higher quantity of unpaired electrons tending to align with an externally applied field, and maintaining the orientation after the external field is removed. The explanation of the ferromagnetic phenomena are due to the energy mechanisms presented in section 2. When applying a current or an external magnetic field, interesting effects such as resonance can be observed in the ferromagnets. Section 3.2 will explain this in detail. The

history and the theoretical foundation behind ferromagnetic resonance will be presented in the following section. Later, in section 7.2, the experimental setup which detects the FMR will be presented in detail.

3.1 History

Ferromagnetic resonance is a spectroscopic technique to measure magnetic properties by detecting the precessional motion of the magnetization in a ferromagnetic sample. It was first discovered by V. K Arkad'yev when he observed the absorption of ultrahigh frequency radiation by ferromagnetic materials in 1911. Landau and Lifshitz [13] provided a theoretical framework from which many of the later results regarding FMR could be derived. The ferromagnetic resonance absorption was officially discovered experimentally by Griffiths [14] in Oxford in 1946. The initial theoretical formulation of FMR was provided by Kittel in 1951 [15]. Since then, huge amount of work has been published describing FMR in various materials in different geometries. Quantitative information about the magnetic properties of materials has been obtained.

3.2 Magneto dynamics

In a ferromagnetic ensemble, the magnetization $\vec{M}$ is taken by simply equating with a sum of non-interacting spins $\vec{\mu_s}$. The time-evolution is

$$\frac{\mathrm{d}\vec{M}}{\mathrm{d}t} = \gamma \vec{M} \times \vec{H} \tag{3.1}$$

where γ is the electron gyromagnetic ratio and $\vec{H}$ is an external static magnetic field. The rate of change in $\vec{M}$ is perpendicular to the plane spanned by $\vec{H}$ and $\vec{M}$. The torque causes $\vec{M}$ to precess around $\vec{H}$ according to figure 3.1, analogous to a spinning top in a gravitation field.

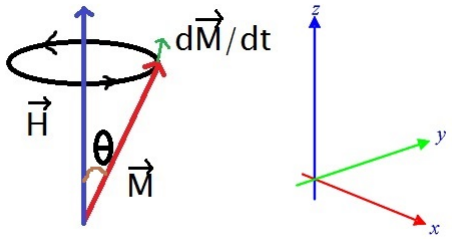

Figure 3.1: Schematic of the magnetization vector $\vec{M}$ precessing around an external field $\vec{H}$

Solving equation (3.1) yields the Larmor frequency:

$$\omega_L = \gamma H \tag{3.2}$$

The Larmor frequency is the governing principle behind important spectroscopy techniques such as nuclear magnetic resonance (NMR), electron paramagnetic resonance (EPR) and *ferromagnetic resonance* (FMR).

To study the response of a system such as (3.1), an oscillating field component with

harmonic time dependence is added to the static field and the magnetization

$$\begin{aligned} \vec{H} &= \vec{H}_0 + \vec{h}e^{i\omega t} \\ \vec{M} &= \vec{M}_0 + \vec{m}e^{i\omega t} \end{aligned} \tag{3.3}$$

where we assume $h \ll H_0$ and $m \ll M_0$, and the static fields to be parallel and oriented along the $\hat{z}$-axis. This is the idealized case of a lossless, isotropic magnet. Substituting equation (3.3) into equation (3.1) and linearizing (setting the products of the ac components to 0), the coupled expressions can be written in the form

$$i\omega t \begin{bmatrix} m_x \\ m_y \\ 0 \end{bmatrix} = \gamma M_0 e^{i\omega t} \begin{bmatrix} -h_y \\ h_x \\ 0 \end{bmatrix} + \gamma H_0 e^{i\omega t} \begin{bmatrix} m_y \\ -m_x \\ 0 \end{bmatrix} \tag{3.4}$$

The solution of equation (3.4) was first presented by Polder [16]

$$\begin{aligned} m_x &= \chi_{xx} h_x + i\chi_{xy} h_y \\ m_y &= \chi_{yy} h_y - i\chi_{yx} h_x \\ m_z &= 0 \end{aligned} \tag{3.5}$$

with the frequency dependent susceptibilities

$$\chi_{xx} = \chi_{yy} = \frac{\gamma^2 H_0 M_0}{(\gamma H_0)^2 - \omega^2} \tag{3.6}$$

$$\chi_{xy} = -\chi_{yx} = \frac{\gamma M_0 \omega}{(\gamma H_0)^2 - \omega^2} \tag{3.7}$$

There are two important points from equations (3.6) and (3.7). Firstly, χ_{xx} and χ_{xy} both grow to infinty when the static field H_0 or excitation frequency ω approach the pole $\omega = \gamma H_0 = \omega_0$. This is the phenomena *ferromagnetic resonance*, *i.e* the resonant absorption of electromagnetic energy in a ferromagnetic sample. With the approximations used in this model, we get resonance precisely at the Larmor frequency. Secondly, the induced precessional magnetic moment $\vec{m}$ from equation (3.5) is rotating in the xy-plane perpendicular to $\vec{M}_0$ and $\vec{H}_0$, as shown in figure 3.2.

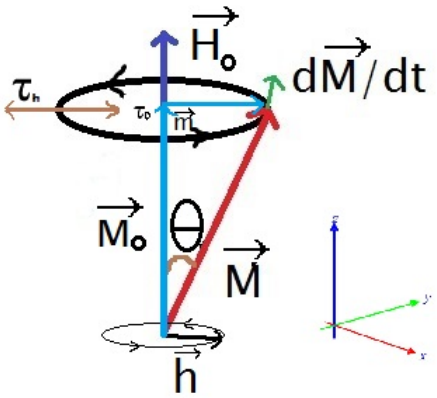

Figure 3.2: Schematic of a magnetic moment $\vec{M} = \vec{M}_0 + \vec{m}$ precessing around a static field $\vec{H}_0$ due to the torque $\mathrm{d}\vec{M}/\mathrm{d}t$. The time-varying field causes an additional torque $\vec{\tau}_h$, which at resonance increases the precession of the magnetization vector $\vec{M}$. A damping torque $\vec{\tau}_D$ acts in the opposite direction. When $\vec{h} = 0$, $\vec{M}$ will eventually end up parallel to $\vec{H}_0$.

The diverging susceptibilities are not physical, but merely a product of an undamped system. The precession of the magnetic moments $\vec{M}$ will relax through dissipation of energy into the material and finally be aligned along the static magnetic field H_0. Landau, Lifshitz and Gilbert brought the dynamical description a step closer to reality by adding a damping term to equation (3.1):

$$\frac{\mathrm{d}\vec{M}}{\mathrm{d}t} = \gamma(\vec{M} \times \vec{H}) + \frac{\alpha}{M}(\vec{M} \times \frac{\mathrm{d}\vec{M}}{\mathrm{d}t}) \tag{3.8}$$

where α is a dimensionless factor referred to as the Gilbert damping parameter. It results in a torque acting on $\vec{M}$ turning it into the direction of $\vec{H}_0$ as shown in figure 3.2. The balance between the driving $\vec{h}$ excitation field and damping determines the angle θ and magnitude of $\vec{M}$. Solving equation (3.8) in the same manner as (3.1), it becomes evident that the damping has an effect on the susceptibilities

$$\chi_{xx} = \frac{\gamma M_0(\gamma H_0 + i\alpha\omega)}{(\gamma H_0 + i\alpha\omega)^2 - \omega^2} \tag{3.9}$$

$$\chi_{xy} = -\frac{i\gamma M_0\omega}{(\gamma H_0 + i\alpha\omega)^2 - \omega^2} \tag{3.10}$$

in that they now are complex functions. The susceptibility can now be described by a real and imaginary term $\chi = \chi' + i\chi''$, where the former represents the dispersion or energy in the system, and the latter energy dissipation or loss. The damping also causes the unphysical divergence indicated in equation (3.6) and (3.7) for the undamped system at resonance to vanish. The damping term in equation (3.8) also affects the lineshape; increasing the damping results in lower amplitude and larger linewidth $\Delta\omega$. The imaginary term of the susceptibility then becomes a measure of the relaxation rate of the magnetization, and is normally described by intrinsic and extrinsic inhomogeneities in the magnet and material-specific Gilbert-damping in real systems:

$$\Delta\omega = \Delta\omega_{\mathrm{inhom}} + \Delta\omega_{\mathrm{G}} = \Delta\omega_{\mathrm{inhom}} + 2\alpha\omega \tag{3.11}$$

Relaxation magnitude and mechanisms play a huge role in the field of rf-electronics. Determination of these parameters have become one of the important traits of FMR-experiments.

3.3 The effective field

So far the calculated resonance frequency ω_0 has solely been a function of $H_0\gamma$. We have not taken into consideration the effective anisotropies presented in sections 3.1-3.4. From section 3.3, the demagnitization field is $\vec{H}_D = -\hat{N}\cdot\vec{M}$. This correction is added to equation (3.3) such that

$$\vec{H}_{\text{int}} = \vec{H}_0 - \hat{N}\cdot\vec{M}_0 \tag{3.12}$$

$$\vec{h}_{\text{int}} = \vec{h} - \hat{N}\cdot\vec{m} \tag{3.13}$$

Deriving the susceptibilities with the same procedure as before, an expression for the resonance frequency including the demagnetization factors, first derived by Kittel [15] is obtained

$$\omega_0 = \gamma\sqrt{[H_0 + M_0(N_x - N_z)][H_0 + M_0(N_y - N_z)]} \tag{3.14}$$

which strongly depends on the magnetization geometry of the system. Kittel also proceeded to deal with the magnetocrystalline anisotropy in a similar fashion by introducing effective fields. The static magnetic configuration can be obtained by minimizing the total energy of the system. This energy can be considered to act as an effective field on the magnetization

$$\vec{H}_{\text{eff}} = -\frac{1}{V}\frac{\partial E_{\text{tot}}}{\partial \vec{M}} \tag{3.15}$$

and thus Kittel included both the demagnetization and anisotropy field corrections in an effective demagnetization tensor $\hat{N}_{\text{eff}}$. By substitution into equation (3.14), these effective tensors yields the resonance condition including the magnetocrystalline anisotropies.

3.4 Smit-Suhl approach for the Resonance field position

Another approach to derivation of the resonance frequency was taken by Smit, Beljers and Suhl [17]. They solved equation (3.8) in the spherical coordinate system in a small amplitude approximation. The Smit-Suhl formula is

$$\omega_0 = -\gamma\vec{H}_{\text{eff}} = \frac{\gamma}{M\sin\theta}\sqrt{E_{\theta\theta}E_{\phi\phi} - E_{\theta\phi}^2} \tag{3.16}$$

where $E_{\theta\theta}$, $E_{\phi\phi}$ and $E_{\theta\phi}$ are the double derivatives of the total energy with respect to the spherical coordinates taken at the equilibrium position of $\vec{M}$. Therefore, in order to find the resonance frequency for a given system, an explicit expression for the free energy as a function of magnetization is needed. Looking back at section 2, the expression can be in many cases written as

$$E_{\text{tot}} = E_{\text{anis}} + E_{\text{uniaxial}} + E_{\text{Interface}} + E_{\text{Zeeman}} \tag{3.17}$$

Yuan *et al* conducted a FMR study on single layer Py and Py/FeMn-bilayer films in 2004 [18]. The total magnetic free energy for the film is:

$$\begin{aligned} E_{\text{tot}} = (2\pi M_{\text{FM}}^2 t_{\text{FM}} - K_S)\cos^2\theta - K_U t_{\text{FM}}\sin^2\theta\cos^2\phi - H_E M_{\text{FM}} t_{\text{FM}}\cos\phi \\ -H M_{\text{FM}} t_{\text{FM}}(\sin\theta_H\sin\theta\cos(\phi-\phi_H) + \cos\theta_H\cos\theta) \end{aligned} \tag{3.18}$$

using the coordinate system in figure 3.3. M_{FM} is the magnetization for the Py-layer, t_{FM} the thickness, H is the applied magnetic field, K_U is the in-plane anisotropy constant and

K_S is the interfacial uniaxial anisotropy constant. The first and second term in equation (3.18) represent the sum of the shape anisotropy, and the in-plane uniaxial anisotropy energies respectively. The third term is the FM/AFM exchange coupling energy, while the last term refers to the Zeeman energy (E_{Zeeman}). ϕ_H is the azimuthal angle of the applied field. The expression for the total free energy E_{tot} is then inserted into Smit-Suhl's formula

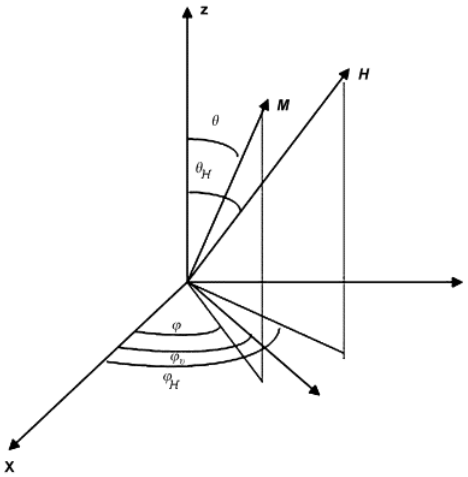

Figure 3.3: The coordinate system in this work. The thin film lies on the xy-plane, which implies that $\theta = \pi/2$ Figure from [19]

(equation (3.16)), with the derivatives taken with respect to the equilibrium positions (θ_0, ϕ_0) of the magnetization. The external field is applied in the thin-film plane (xy-plane), the same plane as $\vec{M}$, meaning we can simplify equation (3.18) by setting $\theta = \pi/2$. The following expression is obtained:

$$\begin{aligned}\left(\frac{\omega_0}{\gamma}\right)^2 = &\left[H_{\text{res}}\cos(\phi_H - \phi_0) + H_S + H_E^{\text{FMR}}\cos\phi_0 + H_K\cos 2\phi\right] \times \\ &\left[4\pi M_{\text{eff}} + H_S + H_{\text{res}}\cos(\phi_H - \phi_0) + H_E^{\text{FMR}}\cos\phi_0 + H_K\cos^2\phi_0\right]\end{aligned} \tag{3.19}$$

where the effective magnetization is $4\pi M_{\text{eff}} = 4\pi M_{\text{FM}} - 2K_S/t_{\text{FM}}M_{\text{FM}}$, the uniaxial anisotropy field $H_K = 2K_U/M_{\text{FM}}$ and H_E^{FMR} is the FMR-exchange bias field. A shifted field, H_S, is introduced. This field is to take into account the permalloy-spin pumping, which gives a shift in the resonance field. This will be explained further in section 5.

As shown in this master work, along with other studies [8, 18, 19], $4\pi M_{\text{eff}} \sim 8\text{kOe}$, $H_{\text{res}} \sim 1\text{kOe}$ and $H_K, H_E^{\text{FMR}} \sim 10\text{Oe}$. We then have the conditions $4\pi M_{\text{eff}} \gg H_{\text{res}} \gg H_K, H_E^{\text{FMR}}$, so that the resonance field can be simplified and expressed as

$$H_{\text{res}}(\phi_H) \simeq \frac{(\omega_0/\gamma)^2}{4\pi M_{\text{eff}}} - H_S - H_E^{\text{FMR}} \cos\phi_H - H_K \cos 2\phi_H \tag{3.20}$$

The average value of the resonance field is $H_{\text{res}} \sim (\omega_0/\gamma)^2 (4\pi M_{\text{eff}})^{-1} - H_S$.

3.5 Temperature effect on the resonance field position

In this work, temperatures in which Bloch's $T^{3/2}$ law (equation (2.12)) is valid has been investigated. Kuanr *et al* [20] showed that the resonance field position H_{res}, in the limit where the applied field H is much smaller than $4\pi M_{\text{eff}}$, also obeyed Bloch's $T^{3/2}$ law:

$$H_{\text{res}}(T) = H_{\text{res}}(0)(1 + bT^{3/2}) \tag{3.21}$$

With $H_{\text{res}}(0)$ being the resonance field position at zero temperature, and b Bloch's constant, as in equation (2.12). In Kuanr's [20] study of epitaxial Fe thin films of 6 and 16 nm, he found that the higher value of $H_{\text{res}}(0)$ in the 6 nm was due to the reduced magnetization.

3.6 Resonance line width

The second term in the LLG-equation (3.8) describes the intrinsic damping of the system. From the macroscopic point of view it reflects the viscous damping of the magnetization motion excited in FMR. It is also a measure of the microscopic mechanism by means of which the absorbed microwave energy is dissipated from the spin system to the lattice vibrations. The Gilbert damping parameter α is dependent on the temperature and it may exhibit anisotropy. The Gilbert damping term leads to a frequency-dependent resonance linewidth ΔH [11, 19],

$$\Delta H = \frac{2}{\sqrt{3}} \frac{\alpha}{M^2 |\partial\omega/\partial H|} \left[E_{\theta\theta} + \frac{1}{\sin^2\theta} E_{\phi\phi} \right]_{\theta_0,\phi_0} + \frac{\partial H_R}{\partial \phi_u} \Delta\phi_u + \Delta H(0) \tag{3.22}$$

where $|\partial\omega/\partial H|$ is the derivative of the resonance frequency with respect to the applied field calculated at the equilibrium position. The first term represents the homogeneous broadening due to the intrinsic conduction mechanism. The second term is introduced to take into account the contribution from the angular dispersion of the uniaxial axis, $\Delta\phi_u$, and $\Delta H(0)$ is a frequency independent term which takes into account the inhomogenouses in the sample. Calculating the derivatives of E_{tot} again with the condition $4\pi M_{\text{eff}} \gg H_K$, the following expression for ΔH is obtained

$$\Delta H \simeq \frac{2}{\sqrt{3}} \frac{\alpha}{M} + 2H_K \sin 2(\phi_H) \Delta\phi_u + \Delta H(0) \tag{3.23}$$

The average value of the resonance width is then $\Delta H \sim (2/\sqrt{3})(\omega/\gamma^2)/M + H_u \Delta\phi_u + \Delta H(0)$. Due to spin pumping, an enhancement in the Gilbert damping constant α is expected. This will be explained and discussed in section 5.

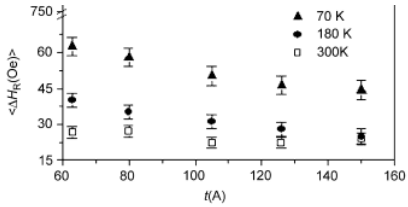

Figure 3.4: Thickness dependence of ΔH at the temperatures 77, 180 and 330 K. Experimental results from [19].

3.7 Temperature effect on the resonance width

Several experiments on the temperature effect of ΔH has been performed and the results will be presented here. Diaz *et al* [19] studied permalloy films with thickness from 6 to 15 nm at the temperatures 77, 180 and 330 K. The results for the resonance width are given in figure 3.4 A decrease in ΔH can be found for increasing temperatures. Similar behaviour can be found from Kuanr's experiments [20] on 6 and 16 nm epitaxial Fe thin films.

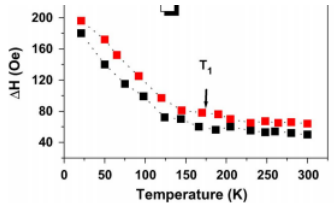

Figure 3.5: Resonance width ΔH as a function of temperature for 6 nm (red points) and 16 nm (black points). Experimental results from [20].

From figure 3.5 we see a linear decrease in the line width up to $T = 180$K. From $T = 180 - 300$K we see that ΔH is almost independent of temperature.

4 Antiferromagnets

A material that exhibits antiferromagnetism [9], has neighboring spins aligned anti-parallel to each other, as shown in figures 4.1 and 4.2. The exchange integral J_{ij} from equation (2.2) in an anti-parallel configuration is less than zero. Often this occurs in systems which can be considered as two interpenetrating sublattices, on one of which the spin points up, and one of which the spins point down. The nearest neighbours of each spins will then entirely be on the other sublattice. Generally, antiferromagnetic order may exist at sufficiently low temperatures, vanishing above a certain temperature, the **Néel Temperature**. Above the Néel temperature T_N, the material is paramagnetic.

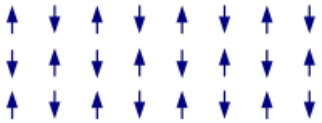

Figure 4.1: Two-dimensional spin ordering of an anti-ferromagnet below T_N. The exchange integral from (2.2) is less than zero.

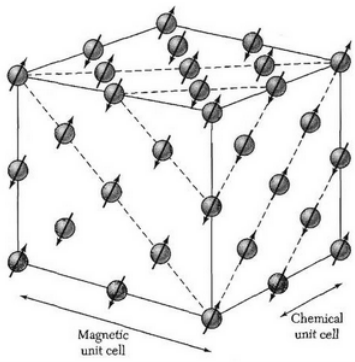

Figure 4.2: Spin ordering of the anti-ferromagnetic compound MnO from [9]. The arrows at each atomic site denote the direction of the spin. The spins in the [111] parallel, while the spins in the adjacent [111] planes are anti parallel. Thus MnO is an antiferromagnet.

4.1 Antiferromagnetic materials

Antiferromagnetic materials occur commonly among metal-oxides transition metal compounds. Examples include hematite, metallic oxides, metals such as chromium and alloys such as . The T_N's and anisotropies of metallic AFM materials are generally higher than AFM-oxides. For these reasons, they are preferred for most applications, and their behaviour in FM/AFM couplings has been extensively investigated. The metallic AFM materials have generally been Mn alloys. Hempstead *et. al* [21] reported that Mn alloys with Ni, Rh and Pt are useful γ-phase AFM materials for producing unidirectional properties. One example of an AFM spin-ordering is figure 4.2. Generally there are many ways of ordering the spins in a three-dimensional structure in order to get an AFM, as long as the net magnetic moment is zero below T_N.

4.2 Exchange bias

Antiferromagnets can couple to ferromagnets through a mechanism known as *exchange bias*, in which a ferromagnetic film is grown upon the antiferromagnetic film. The effect of the exchange bias is to produce a unidirectional exchange field $\vec{H}_E$ which can act in competition with the applied field $\vec{H}$. When $\vec{H}$ and $\vec{H}_E$ are in the same direction, the effect is a shift of the hysteresis loop. This effect can be used to pin the magnetization direction of a soft ferromagnet which is grown upon an antiferromagnet, as shown in figure 4.3.

The exchange bias can be set by cooling the system with an external field (also called field cooling) through T_N of the antiferromagnet. However, challenges regarding oxidation of the material arises. A good capping material which can withstand temperatures well above T_N is needed. The exchange field between the ferromagnetic and antiferromagnetic layer is poorly understood due to the difficulty in studying the domain walls in thin antiferromagnetic films. The first term in equation (2.8), depends on knowing the spin structure in the AFM film. There are methods to engineer the domains, as well as characterization. Logan *et al* [22] engineered a domain wall by depositing a thin iron cap-layer on a 300 nm chromium film. By etching selected areas of the iron cap, a domain wall arised, where the spin polarization was different than the area which was capped.

The total magnetic moment of an antiferromagent is zero. But on the surface, there lies uncompensated spins, creating exchange bias when coupled with a ferromagnet. Mapping out the local magnetization throughout the area of the AFM-film can be done by either spin-polarized STM, neutron diffraction or X-ray diffraction. Domain walls can form between regions of different phase, polarization direction and propagation direction. In thin films, domain walls are irregular and come in widely varying shapes and sizes. Additionally, the domains are weakly pinned and subject to thermal and quantum mechanical fluctuations. The challenge is therefore to engineer stable domain walls which allows possibilities to control and map out the properties of the thin-film systems.

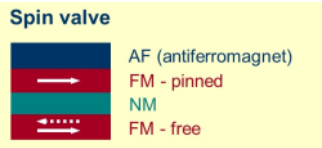

Figure 4.3: A model of a spin valve. The magnetization of the upper ferromagnetic layer is pinned by the antiferromagnet. The magnetization of the lower layer is free to move. The figure is from [23]

4.3 Applications of antiferromagnets: Spin valves and "read-heads"

The exchange bias in a FM/AFM interface can be used to create a *spin valve*, which are the basis of modern hard drive read heads, first introduced by IBM in 1998 [24]. All modern computers use exchange bias in the magnetic thin films sensors that "read" the bits stored on the rewritable magnetic hard disk. Figure 4.4 is a schematic view of a read-write head addressing the recording medium on a hard drive. [1]The recording medium is a magnetic film ∼10-20 nm thick, with high remanence field and coercivity. It is supported on a

[1]Details about the parameters used are from [2]. They are meant to be typical values for a recording head and the parameters does not necessarily correspond to figure 4.4 which is used for illustration purpose

rotating flat disc. The read-write structure is mounted on a lever-arm which is suspended 10-20 nm above the recording medium. Pulsed currents of the writing element produces the magnetic field to write the bits.

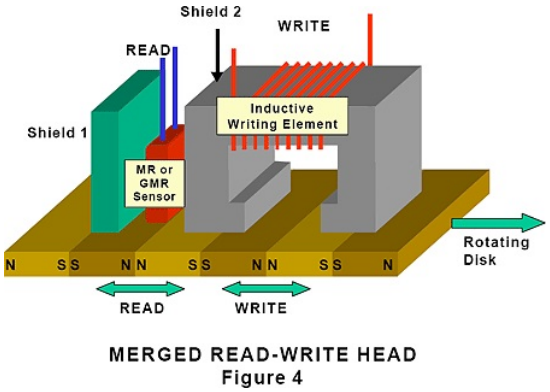

Figure 4.4: Illustration of a "Read-Write" head addressing the magnetic storage film on a hard disk from [25].

The write-element selectively magnetizes small regions in the desired binary code pattern. The 0's and 1's are distinguished by whether the adjacent bits are magnetized in opposite directions or not. When the magnetization direction in the spin valve changes, the resistance changes which gives a read-signal. The resistance change is due to the *giant magnetoresistance* effect and is a large topic in the area of *spintronics* which will be presented in the section 5. This section was meant to give an understanding of a technological application of spin valves, giant magnetoresitance and exchange bias. I refer to [2] and [25] for a more detailed explanation of how the "read-write" head works.

4.4 Antiferromagnetism in Chromium

The antiferromagnetic structure of Chromium was discovered via neutron scattering in 1959 by a Corliss and Hastings [26]. The structure is bcc with the body-centered spin antiparallel to the corner spin as shown in figure 4.5. The Néel temperature of chromium is 311 K [9]. Bacon (1961) [27] found the Néel transistion for a single crystalline sample and a polycrystalline near a temperature at about 313 K. For a heavily crushed powder of chromium, the onset of long-range magnetic order takes place at 450 K [28] An antiferromagnetic structure of type AF_0 (figure 4.9) takes place below this temperature. This AF_0 phase was recognized to be associated with strain in the heavily crushed Cr powder sample.

The Néel temperature of 311 K is associated to a relatively unstrained sample, as a single crystalline and poly-crystalline sample. These samples undergo another phase transition at 123 K, the spin-flip transition temperature T_{SF} (presented in section 4.5.4). By studying the neutron diffraction peaks of the phases, Bacon and Cowlam [28] were able to characterize the temperature dependence of the AFM structures in coarse powder and fine powder chromium. The results are given in figure 4.10

There are two special properties of Cr that are needed to explain it [29]. The first is the *spin-density waves* which is due to nesting of the Fermi surface. The second property is that although the lowest energy state is nonmagnetic, a small expansion of the lattice brings a second-order transition into a type-I antiferromagnetic phase with rapidly rising local moments. The combined properties, which in the following sections will be explained in more detail, provide a mechanism for the unusual antiferromagnetic ground state. The

spin-density wave (SDW), which modulates the moments of the antiferromagnetic phase can be used to compensate the strain energy of the lattice expansion.

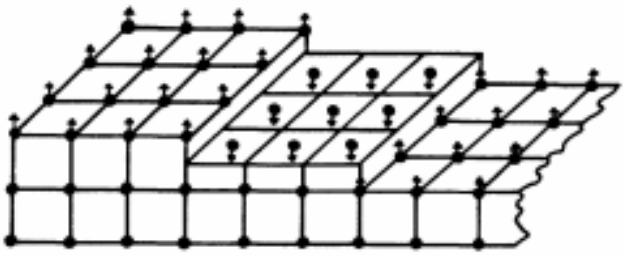

Figure 4.5: Magnetic order at the Cr[001] surface containing monoatomic high steps. Each monolayer is ferromagnetically ordered and antiferromagneticly coupled with the next layer. (from [30])

4.5 Spin-density wave (SDW)

Spin-density waves are broken-symmetry ground states of metals [31], the name referring to the periodic modulation of the spin density with period $\lambda_{\mathrm{SDW}} = \pi/k_F$. The development of the SDW state opens up a gap in the single-particle spectrum. SDWs are thought to arise as the consequence of electron-electron interactions. However, exchange interactions arising from repulsive forces (section 2.3) always favor the parallel alignment of spins. Partial or complete ferromagnetic polarization of an electron gas increases the magnitude of the exchange energy. Ferromagnetic polarization introduces a long-range parallelism as well as a short-range, but it is the latter that is more important with respect to exchange energy.

The simplest of all models is Overhauser's one dimensional gas of electrons [32], having three-dimensional spins interacting via a repulsive delta-function potential. In this model, if one looks for a solution in the form of a helical SDW, one finds a self-consistent Hartree-Fock potential of the form

$$U(z) = g_z[\sigma_x \cos(qz) + \sigma_y \sin(qz)] \tag{4.1}$$

where g_z is a parameter to be determined, q is the wave vector and σ_x and σ_y are Pauli matrices. In order to obtain the lowest, the wave vector q of the SDW must be such that the energy gaps occur at the Fermi energy. In this case, the electron states that are raised in energy are not occupied, wheras those states lowered in energy are occupied, thus allowing the SDW to produce an overall reduction in energy. Figure 4.6 shows a unique feature for the single-particle energy spectrum. The energy gap occurs at only one side for a given spin. Near the energy gaps the real spin-directions spiral in a plane perpendicular to the axis of spin quantization.

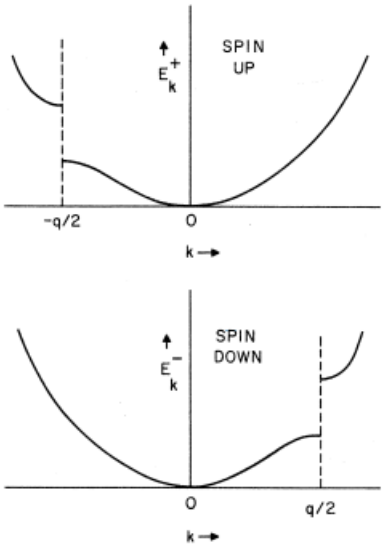

Figure 4.6: Single-particle energy level spectrum for an electron gas with a spiral SDW. From [32]

In three dimensions the question arises whether the SDW is a single q, for example q_3, with q_1 and q_2 equally possible, so one might expect a real single crystal to be multidomain with domains corresponding to q_1, q_2 and q_3 regions. This will be called poly-q, with the three SDWs interpenetrating each other. The stability of the single q SDW for Cr can be seen in figure 4.7. Let us suppose that a helical SDW of wave vector q_3 and positive helicity produces energy gaps on the shaded portions of the Fermi surface. A negative helical SDW with the same wavevector will produce gaps on the remaining portions of the Fermi surface. The linearly polarized SDW sinusodial wave results from a superposition of these two waves alone. The wavevector q_3 was chosen to be along k_z. The important point of figure 4.7 is that all of the Fermi surface is involved in forming a linearly polarized SDW of either wave vector q_3 or q_2, except for the corners of the hole surface in the case when the electron surface is smaller.

A single-q state is to be expected for the two-dimensional Fermi surface as shown in 4.7. The fact that the single-q SDW state is favored in Cr is due to the Fermi surface geometry.

4.5.1 Spin-density wave antiferromagnetism in Chromium

The incommensurate SDW of chromium is characterized by a wave vector $\vec{k}$ determined by the nesting properties of its Fermi surface. Translation between two parts of the Fermi surface vectors by either of two nesting vectors in k-space with wave numbers equally above and below the reciprocal lattice vector in the [001] direction brings large areas of each part of the surface to near coincidence.

One can show [33] that SDW wave-vector $\vec{k}$ can connect two pieces of the Fermi surface, and that the stability of the SDW state is the Fermi surface has the *nesting* property. This means that the electron and hole surfaces can be superposed by translation through the nesting vector $\vec{k}_N$. The magnitude of $\vec{k}_N$ turns out to be essentially the same as that of $\vec{k}$ in a real metal [34].

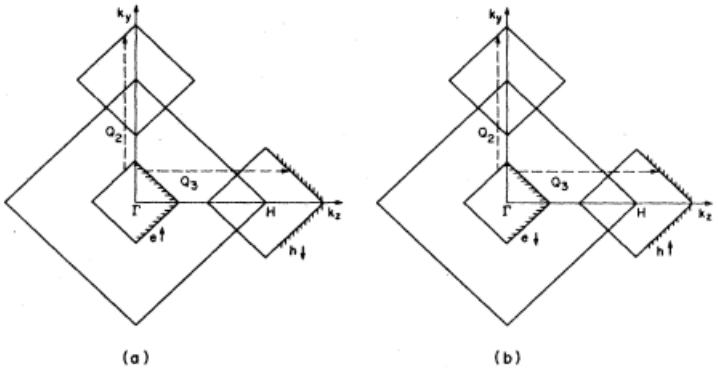

Figure 4.7: Fermi surface for a schematic two-dimensional model of Cr. The first Brillouin zone is duplicated to allow both spin up (↑) and spin down (↓) for electrons (e) and holes (h) to be shown separately. (a) shows $e\uparrow$ and $h\downarrow$, (b) shows $e\downarrow$ and $h\uparrow$. The electron surface is placed on the center Γ of the Brillouin zone, whereas the hole surface is centered on the corner H of the zone.

Overhauser [33] showed that a linearly polarized SDW should have lower energy than a helical SDW. In the ground state of the isotropic Heisenberg model, which is often used to describe localized spin systems, Overhauser's findings were remarkable. Other features

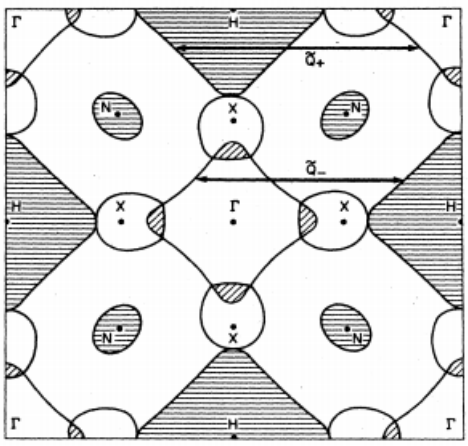

Figure 4.8: Calculated Fermi Surface of a [100] cross-section of Cr. Typical nesting vectors $\tilde{Q}_\pm = (0, 0, 1 \pm \delta)$, between Γ and H surfaces are shown.

of antiferromagnetism in Cr that needs to be considered are:

- The variation of the energy gap Δ.
- The amplitude g of the SDW and its wave vector q.
- The change in electron-to-atom ratio by alloying Cr with other non-magnetic transition metals, or with the oxidation of Cr.
- The phase diagram showing the regions of AF_0, AF_1 and AF_2 and P (paramagnetic) in the Cr sample.

Extensive theoretical and experimental research has been done throughout the 70's and 80's on the microscopical model of Cr. In this master thesis, the aim is to understand how the magnetic structure of chromium affects resonance profile of a permalloy/copper/chromium/(copper) system.

4.5.2 Antiferromagnetic ordering

Figure 4.9 shows three different spin-ordering types, AF_0, AF_1 and AF_2 for the bcc-structured chromium. The AF_0-structure corresponds to a crushed powder sample with a high degree of internal strain. The AF_1-structure is the the transverse SDW, while the AF_2-structure is the longitudinal SDW.

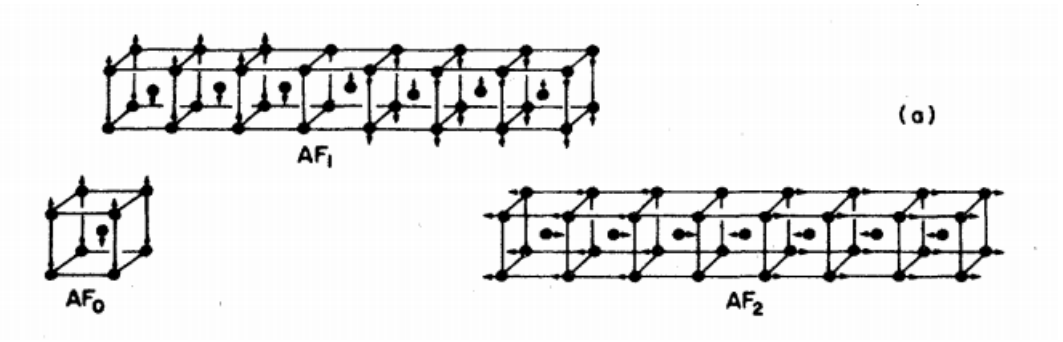

Figure 4.9: The diagrams represent the magnetic structures AF_0, AF_1 and AF_2 which occur in chromium. The arrows show the directions and approximate magnitude of the magnetic moments. From [28]

The transition from the paramagnetic phase to the AF_1 takes place at the T_N. At the spin-flip temperature, T_{SF}, the magnetic structure of chromium transforms from a transverse to a longitudinal spin-ordering. Figure 4.10 shows the magnetic phase diagram for various samples of chromium.

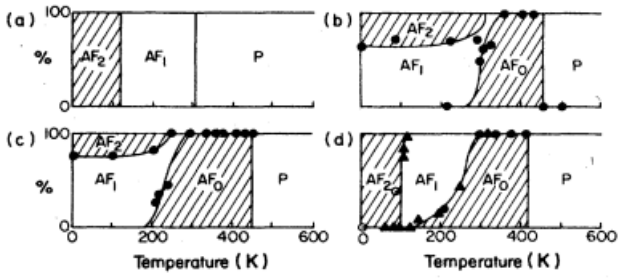

Figure 4.10: The magnetic phase diagram deduced for: (a) ideal single crystal chromium, (b) coarse powder, (c) fine powder of chromium and (d) 99.5% Cr and 0.5% Re-alloy, indicating the extent of occurrence of the magnetic structures AF_0, AF_1 and AF_2 and P (paramagnetic). From [28].

As figures 4.10 (b)-(d) indicates, there is a coexistence of magnetic phases in the samples. The transition between the phases occur over a temperature interval. Bacon and Cowlam [28] also conducted studies of annealed chromium powder at 600°C and 1000°C. The results (compared to figure 4.10) showed that firstly, the AF_0-structure was decreased, along with the reduction of the temperature interval which the AF_0-AF_1 and AF_1-AF_2 occured. The local inhomogeneous, which give rise to the AF_0-phase, gets reduced to the extent of the annealing temperature and duration until it doesn't exist.

4.5.3 Néel transition

The existence of a phase transition at T_N in Cr is observed quite clearly in elastic neutron scattering and in thermal expansion. This transition is weak and intervenes in what appears to be the approach to a continuous transition, as the order parameter decreases

with increasing temperature. Several researchers have attempted to determine the critical parameters for the Néel transitions, but due to the practical difficulties, the determination of the unambiguous values has proved formidable. This is due to the great sensitivity to strain of the SDW near T_N.

The latent heat at the Néel transition is difficult to determine because of the strong stress dependence of the T_N, which results in smearing of the transition in a sample having internal strain due to lattice defects. An estimate of 1.2 ± 0.2 J/mol was made by [34] based on various experiments performed in the 1970s. The total magnetic entropy is even more difficult to estimate, because of the absence of a base-line for paramagnetic Cr to which the specific heat of AFM Cr can be referred.

The effect of an external magnetic field on T_N was determined by Barak *et al.* [35], who employed a capacitance dilatometer to measure the discontinuous length change parallel to the field to signal the Néel transition. T_N was found to be independent of field up to 16 T, well over the magnetic field strength, 0.6 T used in this work.

4.5.4 Spin-flip transition and incommensurate/commensurate SDW

The spin-flip temperature $T_{sf} = 123$ K can readily be described within the framework of a Landau-type model. As discussed in section 4.5.2, the heating of the sample through T_{sf} changes the SDW polarization from the longitudinal AF_2-phase to the transverse AF_1 phase. The fact that the magnetization, but not the $\vec{q}$ vector changes directions at T_{sf} suggests that the single $\vec{q}$-state chromium possesses a uniaxial anisotropy with respect to the $\vec{q}$-direction [36], which lies along one of the cubic axes of the paramagnetic state. The uniaxial anisotropy occurs because $\vec{q}$ is *incommensurate*. If $\vec{q}$ is commensurate, as in chromium alloyed with with manganese, no distinction can be made between the transverse and longitudinal SDW meaning which means that there is no spin-flip transition.

Many features of the spin-flip transition can be described phenomenologically by assuming a uniaxial anistropy term in the free energy in equation (2.7)

$$E_{\text{uni}} = K(T)(\hat{n} \cdot \hat{Q})^2 \tag{4.2}$$

where $\hat{n}$ and $\hat{Q}$ are unit vectors in the direction of the magnetization and $\vec{Q}$ respectively, and K is the temperature-dependent anisotropy constant. $K(T)$ changes from negative to positive as the temperature increases through T_{sf}. The phenomenological analysis leads to the following expression for $K(T)$ in the temperature range 95 K $\leq T \leq T_{sf}$:

$$K(T) = -3.89 \times 10^4 (1 - T/T_{sf}) \text{ erg/cm}^3 \tag{4.3}$$

The theoretical challenge is to demonstrate a microscopic origin of the uniaxial anisotropy for an incommensurate SDW with the right magnitude and proper temperature dependence. Allen and Young (1975) [36] developed a theory where two mechanisms are involved in the uniaxial anisotropy: Magnetic dipole interactions and spin-orbit coupling, both have the same temperature dependence, namely the AFM energy gap squared. Thus a zero crossing of the anisotropy coefficient does not occur.

The magnetic phase diagram near T_{sf} has been mapped out (Barak *et al.* [28]) by observing the peaks in the ultrasonic attenuation which occur at the phase boundaries. Barak *et al.* conducted experiments with different polarizations of the SDW vector $\vec{q}$ relative to an applied field $\vec{H}$ and the ultrasonic propagation direction.

4.5.5 SDW in Chromium with a Cu cap-layer

Bödeker *et al* [37] determined the effect of a 2 nm thick Cu cap layer on the phase diagram of a 200 nm Cr(001) film via neutron scattering. In figure 4.11 the characteristic neutron scans of the sample are shown. The lower left panel shows that a longitudinal SDW is propagating out-of-plane for all temperatures from 15 K to the Néel temperature. Therefore there is no spin-flip transition in the system, contrary to bulk Cr (section 4.5.4).

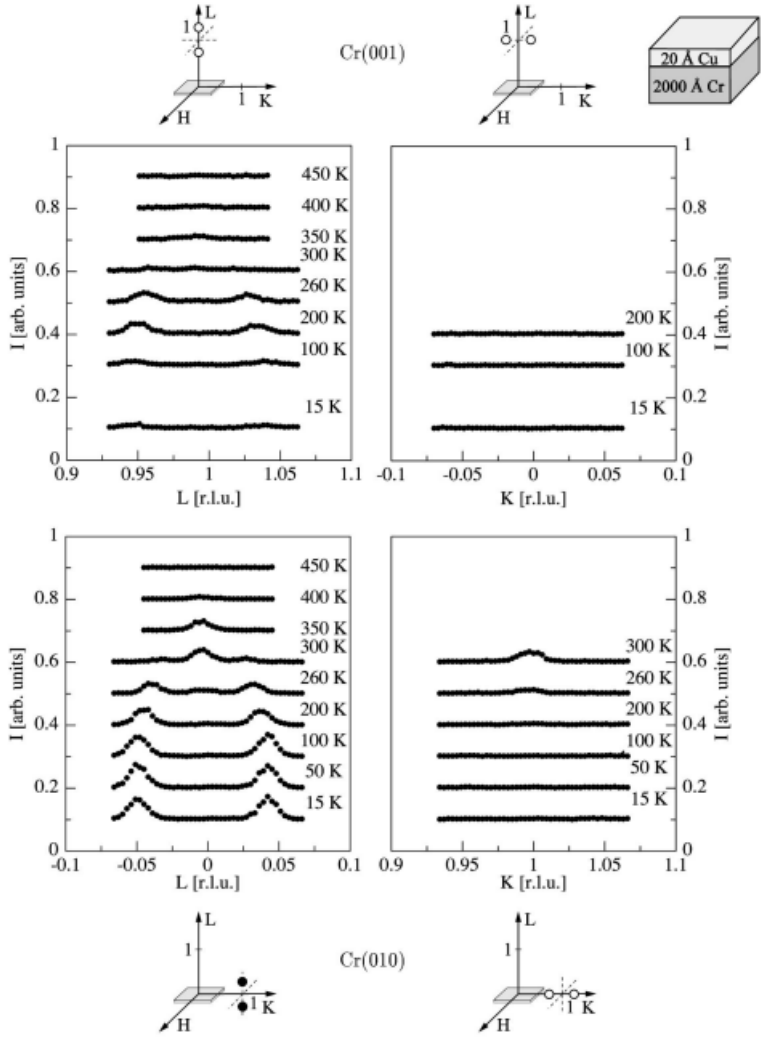

Figure 4.11: Neutron-scattering experiments revealing the SDW in a 200 nm Cr(001) film with a 2 nm Cu cap-layer for temperatures from 15 to 400 K. The figure indicates that the SDW propagates in the out-of-plane direction and has dominantly longitudinal polarization. From [37]

There is no commensurate phase at low temperatures as seen for the ferromagnetic cap layers which also was studied by [37]. The commensurate phase occurs first close to the Néel temperature. A small amount of a transverse SDW propagating in the out-of-plane direction starts at about 100 K. The phase diagram for this sample is shown in figure 4.12. Bödeker *et al* [37] also concluded that a cap-layer of Cu had essentially the same on the SDWs as a Cr/vacuum or a Cr/Cr_2O_3 interface.

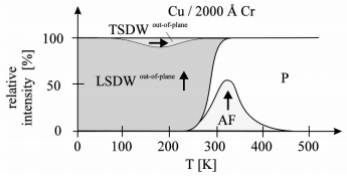

Figure 4.12: Qualitative phase diagram for the commensurate and incommensurate SDW, according to the scattering results shown in figure 4.11. From [37].

4.6 Magnetism of Chromium in thin films

In thin films the magnetism of Cr has become the focus of interest because of its mediating role in exchange coupled superlattices and GMR materials (section 4.3). With the SDW properties and magnetic phase transitions of Cr discussed in sections (4.4-4.5), the question is how the properties are altered in thin films, either due to dimensionality effects or due to the proximity of paramagnetic and ferromagnetic boundary layers. The SDW magnetism in thin Cr films is more difficult to detect experimentally with neutron and x-ray scattering due to small scattering volumes.

Thin films of Cr are also of interest because of predictions concerning their surface magnetic properties. The possibilities of unveiling the intriguing magnetic properties of Cr films and surfaces relies on the capabilities of growing well ordered epitaxial films. Considerable theoretical and experimental efforts has been devoted to the understanding of the SDW order in Cr subject to confined environments and specific boundary layers. The following section will present some of the main results.

For bulk Cr the formation of a SDW arises from the nesting between parallel sheets of the electron and hole Fermi surfaces. In thin films, the interface exchange and hybridization effects may have an important effect on the amplitude and wave vector of the SDW. Thus it's expected that the difference between Cr thin films and bulk is determined by symmetry, proximity and finite size scaling.

4.6.1 SDW in Fe/Cr super-lattices

What happens to the SDW structure of Cr in the vicinity of a ferromagnetic layer is of particularly of interest regarding spin valves and GMR-read-heads (section 4.2). Electronic structure calculations of Fe/Cr super-lattices have been presented by Hirai [38]

A number N of Cr monolayers (ML) on a Fe substrate is considered. The first ML is expected to be ferromagnetically ordered and out-of-plane AF-coupled with the Fe-substrate. The second Cr ML is again F-ordered and AF-coupled with the previous Cr ML, setting up a layered antiferromagnetic structure with a two ML period as in figure 4.5. For thicker Cr layers the first phase slip indicates a transition from the commensurate to an incommensurate SDW. The question arises whether the magnetic order can be sustained for several ML, or whether it decays fast with the number of ML before the intrinsic I-SDW order sets in for a critical number N_c of Cr MLs. If N chromium MLs are embedded in between two ferromagnetic layer, the magnetic order of Cr may depend on whether the magnetization vectors on each Fe-layers are aligned parallel or antiparallel and whether the number of MLs are even or odd as illustrated in figure 4.13.

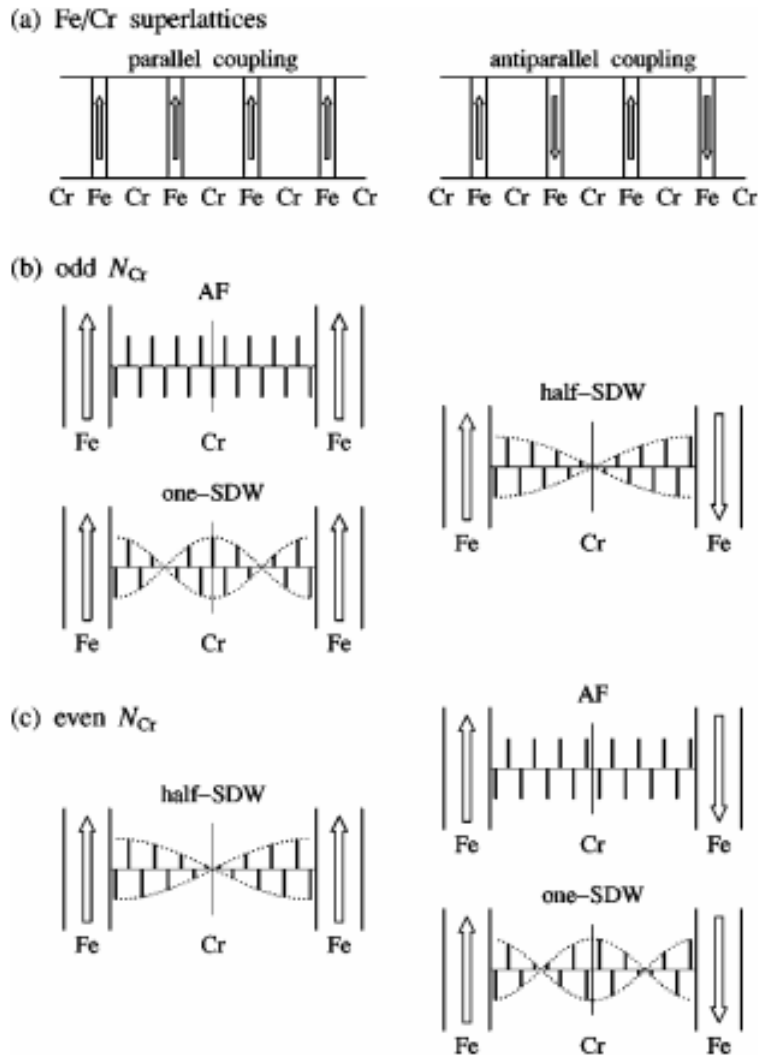

Figure 4.13: Magnetic order in (a) Fe/Cr superlattices and in the spacer-Cr layer for the cases of (b) odd N_{Cr} and (c) even N_{Cr}. An arrow indicates the magnetization direction of an Fe-layer, and a bar indicates the local magnetic moment of a Cr atom. The local magnetic moment of a Cr atom at the interface is antiparallel to the magnetization of the neighboring Fe layer. From [38]

A theoretical study of Cr spin polarization at different Cr thicknesses and temperatures on Fe was conducted by Shi *et al* [39]. Some of their results are plotted in figure 4.14. The energy of the SDW per interface area a^2 can be written [39]

$$E_{\mathrm{SDW}} = A[\vec{\mu_{F1}}\vec{\mu_{Cr}}(1) + \vec{\mu_{F2}}\vec{\mu_{Cr}}(N)] + \frac{1}{2}\Delta F a^3(N-1) \tag{4.4}$$

where A is an interfacial antiferromagnetic exchange coupling and ΔF is the nesting free energy per unit volume of the spacer at temperature T. $\vec{\mu}$ is the magnetic moments of the ferromagnetic layer and each Cr monolayer. The first term describes the proximity to the boundary layers and the second term the intrinsic instability of bulk Cr against the formation of an incommensurate SDW. Figure 4.14, where $J_{\mathrm{Coup}} = E_{SDW} - E_{FM}$ is plotted, shows an oscillation with period 2 ML is shown with a higher amplitude under T_N than over. The amplitude vanishes for a high amount of MLs over T_N. An appearance of nodes is also shown. These results confirmed the experimental results found by Unguris *et al* [40].

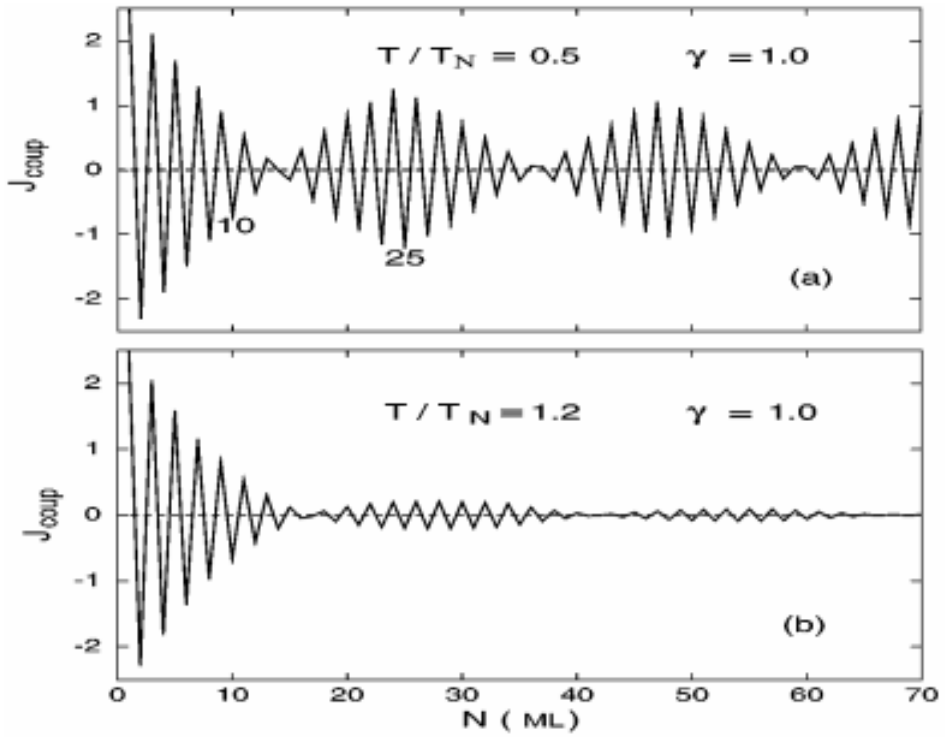

Figure 4.14: Oscillation of the magnetic coupling reflecting the incommensurate SDW in Cr with a number of (001) oriented monolayers. The Cr-layers is in contact with a ferromagnetic layer on both sides. (a) shows the SDW for $T = 0.5\ T_N$. (b) shows the SDW for $T = 1.2\ T_N$. γ is the interface coupling constant. From [39]

Figure 4.15 shows a shift of the oscillation of the SDW amplitude g. This striking feature can be explained by the competition between the interface coupling, which maximizes the SDW amplitude at the boundaries, and the intrinsic antiferromagnetism of the spaces, which favors the bulk values of the SDW amplitude and wave vector. While the SDW gains energy due to the interaction at interfaces, it forfeits energy due to the changes in the order parameters of the spacer. As the spacer thickness increases in figure 4.15, the SDW first stretches to optimize the interface coupling and then suddenly relaxes to lower the bulk free energy. For example, the SDW with $N = 34$ ML (~ 10.0 nm) contains a single node. $N = 52$ ML (~ 14.6 nm) contains two nodes. The nesting free energy per unit volume ΔF is proportional to g^2, the SDW amplitude which is plotted in figure 4.15

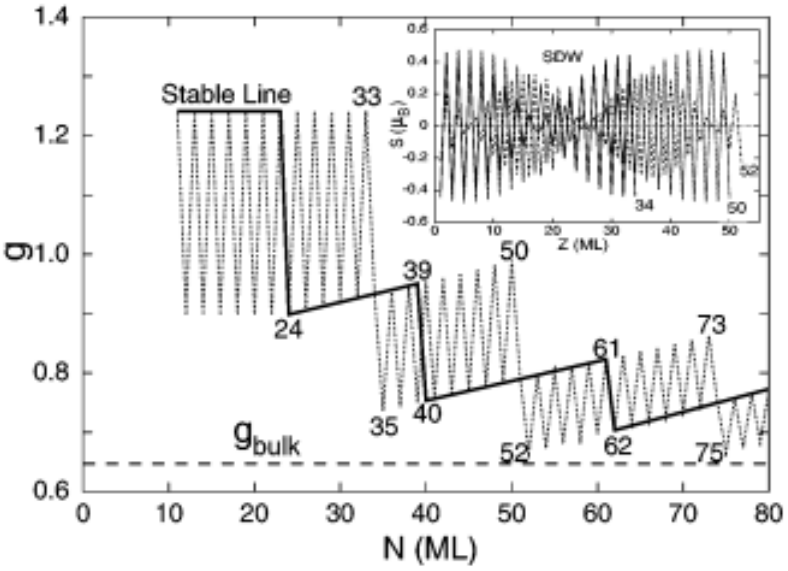

Figure 4.15: SDW amplitude g in units of T_N as a function of spacer thickness for $T = 0.5$ T_N and $\gamma = 2.5$. The dotted line is for ferromagnetic layers, and the solid line is for the stable magnetic configuration with the lowest energy. Inset: SDW profiles in the spacer for $N = 34$ ML (solid), 50 ML (dotted), or 52 ML (dashed) From [39]

One of the main points from Shi *et al*'s work is that the SDW amplitude is larger for $N < 24$ MLs (~ 6.7 nm), and approaches the bulk value for $N \to \infty$. A SDW structure also exists above T_N, indicating a weak AF-structure at higher temperatures. In this work, it should be noted that chromium and the iron-based permalloy film are not in direct contact with each other, but with a 10 nm copper layer in between.

5 Magnetodynamics: Spin-pumping

5.1 Spintronics

Spintronics is an emerging technology which exploits both the intrinsic spin of the electron and its associated magnetic moment in solid-state devices. Modern devices such as transistors, CPUs, LED-lasers and random access memories are examples which uses the principles of spintronics in order to work.

Spin-polarized electron injection from a ferromagnet to a normal magnet (discovered by Johnson and Silsbee in 1985 [41]), as well as giant magnetoresistance (discovered by Fert *et al.* [**?**], Grünberg *et al.* [42] in 1988) are examples of significant discoveries in the field of spintronics. The last 15 years, a lot of research has been devoted to this field in hope to understand the physics better and improve the quality of the devices.

The theoretical foundation of how spintronics is related to ferromagnetic resonance will be presented in the following section. At resonance, the permalloy-film generates a spin-current which propagates through the material.

5.2 Spin waves

In 2004, it was experimentally confirmed by Özyilmaz [43] that a dc-current-driven ferromagnetic layer may undergo a resonant finite-wave-vector spin-wave excitation. The mag-

netization torque is equivalent to absorption of an incident spin current with a polarization component perpendicular to the magnetization. If one neglects the spin-orbit coupling and other spin-flip processes, the total spin angular momentum is conserved. The spin angular-momentum difference between an electron entering and leaving a ferromagnet is therefore transferred to the magnetization. Under a sufficiently large angular-momentum transfer, the magnetization starts to move. The component of the net spin angular-momentum flow out of the ferromagnet $\vec{I}_s$ parallel to $\vec{M}$ vanishes, since the outflow cancels the inflow for the parallel component. The *spin-transfer torque* $\vec{\tau} = -\vec{I}_s$ should be accounted for as an additional source term in the equation of motion for the magnetization. The torque that drives the transverse magnetic dynamics [44]

$$\vec{\tau} = -\vec{M} \times \vec{I}_s \times \vec{M} \tag{5.1}$$

An electron injected at the Fermi energy and transverse polarization is described by a linear combination of up and down spin eigenstates associated with different Fermi wave vectors, $k_F^{\uparrow}$ and $k_F^{\downarrow}$. Fermi-level states entering the ferromagnet at different angles precess at different length scales perpendicular to the interface, depending on the perpendicular component of the spin-up and spin-down wave-vector difference. If the ferromagnet has a large cross-section area, a large number of transverse modes with different precession lengths will contribute to the spin current.

The scale of the transverse-spin coherence length corresponds to the destructive interference of states with different phases inside the ferromagnet

$$\lambda_{sc} = \frac{\pi}{\mid k_F^{\uparrow} - k_F^{\downarrow} \mid} \tag{5.2}$$

where $\lambda_{sc} \sim \lambda_F$ (the Fermi wavelength), which is an atomistic length scale for transition-metal ferromagnets. After transition through a ferromagnetic film with thickness much larger than λ_{sc}, electrons are completely polarized along the magnetization direction.

5.3 Spin pumping by excited ferromagnets

A moving magnetization in a ferromagnet that is in electrical contact with a normal (non ferromagnetic) conductor pumps a spin current into the non-magnetic environment, giving a contribution to $\vec{I}_s$ in equation (5.1). The spin pumping thus leads to an additional source term in equation (3.8). When the pumped spin angular momentum is not quickly dissipated to the normal conductor, a spin accumulation builds up and creates reaction torques due to transverse spin-backflow into the ferromagnet, as seen in figure 5.1. Using energy and momentum conservation, Brataas *et al.* [44] derived the chemical potential of the spin accumulation in the non-magnetic metal to be $\vec{\mu}_s = \hbar\gamma\vec{H}$, where γ is the gyromagnetic ratio for an electron.

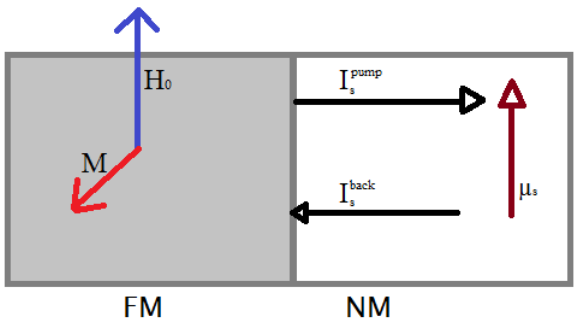

Figure 5.1: The magnetization $\vec{M}$ in the ferromagnetic film rotates around the field $\vec{H}$. In the steady state, the spin pumping $\vec{I}_s^{\text{pump}}$ into the non-magnetic metal cancels the spin backflow $\vec{I}_s^{\text{back}}$ that accompanies the non equilibrium spin accumulaion $\vec{\mu}_s$.

The spin current pumped by a time-dependent magnetization into an adjacent non-magnetic metal is

$$\vec{I}_s^{\text{pump}} = \frac{\hbar}{4\pi}\left(A_r\vec{M}\times\frac{\mathrm{d}\vec{M}}{\mathrm{d}t} + A_i\frac{\mathrm{d}\vec{M}}{\mathrm{d}t}\right) \tag{5.3}$$

where the coefficients A_r and A_i depend on mixing and interface conductances of the FM/NM-system and determines the magnitude of the spin pumping as a function of device parameters. Equation (5.3) is derived in [44]. When the the ferromagnet is thicker than the coherence length defined by equation (5.2), the spin pumping currents originates from the interface since the mixing conductances vanishes. This means that the spin-flip scattering inside the ferromagnet can be disregarded during the spin pumping, which is typically the case in real materials.

5.4 Spin waves at interfaces

Thin films often consist of multiple layers of different materials. Spin waves are created in ferromagnets, can propagate through various materials either with their polarization unchanged or changed. At surfaces between ferromagnets and non-ferromagnets/anti-ferromagnets, the spin waves can either be transmitted or reflected back.

Although reflected electrons hardly penetrate the ferromagnet (above the Fermi wavelength), the strong exchange field can still induce a significant precession of the reflected component. Figure 5.2 shows three different spin states propagating from a NM towards an interface of an FM. Stiles and Zangwill [45] showed that the transverse components $\vec{I_{xx}}$ and $\vec{I_{yx}}$ get absorbed at the interface and leads to a spin-transfer torque in the ferromagnet near the interface. This must be accounted for in equation (5.3). There is no torque associated with the transport of the longitudinal component $\vec{I_{zx}}$. However, in transition-metals like permalloy, this contribution typically is small [46].

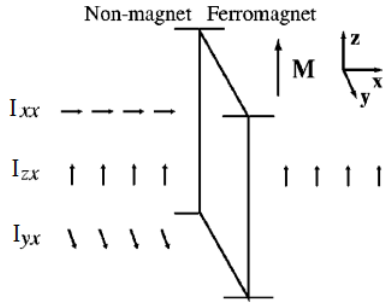

Figure 5.2: Three states of spin-current scatter from an interface. The current flows from the non-magnet to the ferromagnet. $\vec{I_{zx}}$ is parallel to the magnetization of the ferromagnet $\vec{M}$, while $\vec{I_{xx}}$ and $\vec{I_{yx}}$ are transverse to $\vec{M}$. The transverse spin currents are absorbed at the interface. Figure from [45]

5.5 Spin diffusion

In a diffusive conductor, we can define a spin diffusion length λ which is the distance over which a non-equilibrium spin population can propagate without the polarization being changed. Spins of opposite alignment can be treated independently with negligible interaction within λ. The diffusion length depends on the material, but for metals, it is relatively short. If the film thickness is larger than λ, mechanisms such as scattering plays in. Therefore, films of only a few nanometers are required to ensure spin diffusion of known polarization.

Spin pumping and back-flow is a source of viscous damping of the magnetization dynamics in thin films. By conservation of angular momentum, spins ejected out of the ferromagnet exert a transverse reaction torque according to equation (5.1) which is added as an additional source term to equation (3.8) . Solving (3.8) with the source term recovers a new damping constant α_{eff} and a gyromagnetic ratio γ_{eff} which depends on the coefficients A_r and A_i. The interpretations of these coefficients along with the derivation of α_{eff} and γ_{eff} are found in [44]. The main conclusion from the derivation is that spin pumping affects FMR experiments as a shift of the **resonant magnetic field and an increase in resonance linewidth** (from enhanced Gilbert damping) according to equation (3.11). Both effects are accounted for in equations (3.20) and (3.23).

6 Film growth: Sputter deposition

Sputter deposition is a method of depositing thin layers of a material onto a substrate or onto previous deposited layers. It is a physical vapour deposition (PVD) method which deposits the condensation of a vaporized form of the desired thin-film material onto a surface [47]. During sputter deposition, energetic ions (usually argon) from the plasma of a gaseous discharge bombard a target material that is the cathode of the discharge. Target atoms are ejected and gets deposited on a substrate (the anode), forming a coating. The instrument used in this work is AJA Custom ATC-2200V [48]. This chapter will provide a physical understanding of sputter deposition with regards to the instrument used in this work.

6.1 Plasma

A plasma is a partially ionized gas. It consists of charged particles: positive ions and negative electrons. Some plasmas are also *glow discharges*, in that they glow with light emissions from excited atoms. Within plasmas relevant to sputter deposition, the ion and electron densities are essentially equal.

6.2 DC Sputtering

Figure 6.1 shows the essential arrangements for direct current sputter deposition with a parallel-plate charge. The target cathode has a diameter of 2 inches, while the substrate anode has a diameter of 4 inches. The DC source has a maximum operating effect of 300 W. This is to assure that the target material stays intact. Argon, which is used in

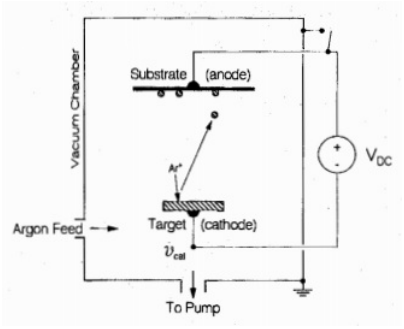

Figure 6.1: DC Sputtering utilizes a gaseous discharge. Argon ions strike the target which deposits atoms to the substrate (anode). The figure is from [47].

this work, is the most common sputtering gas. The pressure used to strike plasma on the targets was 30-60 mTorr, and was reduced to 3-5 mTorr under deposition. The plasma is created and sustained by the DC source via mechanisms that pertain to the abnormal glow regime. Argon atoms flows into the chamber and get ionized when colliding with free electrons. The ions then get bombarded onto the target which leads to ejection of atoms from the surface.

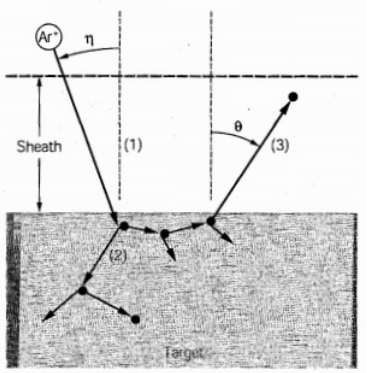

(a) (1) Argon ions are accelerated to the target (negative cathode), (2) an atomic collision between argon and the target material, which leads to (3) ejection of a target atom. The figure is from [47].

(b) The target-plasma is lit and the deposition is under way.

The *sputter yield* is the average number of ejected atoms per incident ion. The maximum possible projectile energy corresponds to the potential difference between the plasma V_p and the cathode V_c

$$E = q(V_p - V_c) \tag{6.1}$$

where q is the electron charge. The particles emitted are predominantly neutral atoms in the ground state, but the target may emit ions and clusters as well.

7 Experimental setup, method and data analysis

7.1 AJA Custom ATC-2200V Sputter

The thin-films used in this work was grown in NTNU NanoLab using the AJA Custom ATC-2200V Sputter [48]. It consists of 5 sputter guns, where one source was RF and the others were DC. The deposition chamber has a base vacuum of $5{\cdot}10^{-8}$ Torr. The deposition thickness is controlled by a quartz crystal monitor. Minimum controlled deposition is ~ 1 nm and maximum is several micrometers. The deposition rate can be varied from ~ 0.1 nm/s to ~ 20 nm/s depending on the target material and the amount of power from the DC/RF sources.

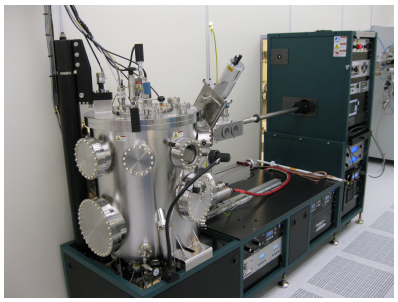

Figure 7.1: The instrument [49] in NTNU NanoLab used to grow the thin films.

7.1.1 Method

Before deposition on the wafers, some testing was required to assure that everything worked the way it was supposed to. The stability of the plasmas on each of the three target materials were tested. Oxidation on the surface of the materials, made the plasmas unstable. Striking the plasmas was also a problem. The solution was to increase the argon-pressure and open the shutters. The increased flow of argon help light the plasma and remove the oxide layer. When the plasma was stable (which was checked by looking into the vacuum chamber), we were able to get a reading on the deposition rate. The quartz crystal monitor was placed directly below the sample holder. The correct film settings were selected on the deposition controller software. When plasma was lit and stable, the shutter was opened and sputtering on the rate monitor occured. In order to get an accurate reading, the deposition lasted 60 seconds. The displayed thickness on the software was divided by 60, and the deposition rate was registered. This was done for each of the three materials. The wafers were also cleaned using O_2 etch plasma. After the rate measurements, the sample-substrates were prepared with a size of $\sim$5 x 5 cm and placed on the sample-holder. The substrate was an n-doped Si-wafer with 30 nm of SiO_2 on the surface provided by my supervisor.

The sample was then loaded into the deposition chamber. Before deposition, the substrate rotation was turned on (in order to ensure uniformity). The Argon flow was turned on and set to 67 sccm with 30 mTorr pressure. In order to strike plasma on the target, the power was set to 50 W. After ensuring the stability of the plasma, the pressure was tuned down to 3 mTorr. The power was ramped up to the value according to table 1.1. After the desired power was reached, the source shutter was opened and kept open until the desired thickness was reached. Afterwards, the power was ramped down to 50 W, and the plasma was shut down. After the desired thin films were created, they were ready to be investigated in the EPR Spectrometer.

7.2 Bruker Elexsys E500 system

The experiments in this work was conducted on a BRUKER ELEXSYS E500 system [50]. The system consisted of:

- A magnet, which could be varied between 0 and 7000 Gauss.
- A temperature system, when filled with liquid nitrogen, could reach temperatures down to 120 K.
- A microwave source, which radiated at about 9.59 GHz.
- A goniometer, which allowed the cavity to rotate.
- A Linux-based control system software.

FMR is based on the collective precessions of spins under the influence of a static magnetic field combined with the absorption of electromagnetic waves, as presented in section 3. The instrumental setup of the experiment is as follows (figure 7.2). A source supplies microwaves into a resonant cavity, which is carefully impedance matched to the waveguide connecting them. By tuning the spectrometer, the cavity will absorb most of the microwave energy at the resonant frequency ω of the sample, and very little reflected signal is measured at the detector diode. The cavity is constructed in such a way that only the magnetic component of the standing microwave is overlapping the sample.

(a) (b)

Figure 7.2: a) A schematic of the cavity based FMR setup. b) A photograph of the system used in the experiment, with the microwave source to the left and the magnet to the right.

During a sweep, the sample is constantly irradiated at the resonance frequency, while the static magnetic field can be varied from 0 to 7000 Gauss. The step-sizes could be varied in order to secure a higher resolution. The recorded absorption curve, given by the imaginary, dissipative term presented in section 3.2; $\chi = \chi' + i\chi''$ can be described by a Lorenzian lineshape (section 7.3), as done in this master work. It is a symmetric profile found in ferromagnets.

7.2.1 Temperature controller, ER 4131VT

The digital temperature control system, ER 4131VT [51] uses liquid nitrogen as a coolant. The accessible temperature range is 120-500K. The system consists of a digital temperature and gas flow unit, thermocouple, and a nitrogen evaporator heater assembly. The digital control unit monitors and controls the temperature measured with the thermocouple close to the sample's position. The target temperature is reached and stabilized with a PID-controller. The whole control unite is regulated on the Xepr software.

7.3 Dysonian lineshape

To obtain a strict and more accurate FMR condition, an iterative fitting procedure is included. First the raw absorption derivative obtained from the FMR-experiment are fitted to Dysonian derivatives [52] describing both the dispersive and absorptive parts of Lorentzian line-shapes,

$$\frac{dP}{dH} = \frac{d}{dH}\left(\frac{\Delta H + \alpha(H - H_{\text{res}})}{4(H - H_{\text{res}})^2 + \Delta H^2} + \frac{\Delta H + \alpha(H + H_{\text{res}})}{4(H + H_{\text{res}})^2 + \Delta H^2}\right) \tag{7.1}$$

where ΔH is the linewidth, α the asymmetry factor and H_{res} the resonance field. The extracted parameters are stored as a function of angle and temperature.

7.4 Fourier Analysis

The extracted parameters, ΔH and H_{res} were periodic with the in-plane angle θ_H. As the results for the raw data will show, some of the parameters had noise. Certain frequency components were filtered out, and the data set was inverse transformed back to re-assemble the noise-free profile.

The relevant functions and analysis in Matlab will be presented here. I refer to [53] for a more comprehensive treatment of Fourier analysis.

7.4.1 Method

In total, 90 data points (at the angles $\theta = \{0°, 4°, 8°, ..., 356°\}$) from each experiment was measured and fitted with the Dysonian lineshape (section 7.3). The discrete signals from ΔH and H_{res} can be represented as $x[n]$ where $n = 0, ..., L-1$ with $L = 90$ (number of datapoints). The discrete Fourier transform (DFT) of $x[n]$ is

$$X(e^{i\omega}) = \sum_n x[n]e^{-i\omega n} \tag{7.2}$$

where $\omega = 2\pi k/L$ (with $k = 0, ..., L-1$) are the discretized frequencies which go from 0 to $2\pi(L-1)/L$. The Matlab command *fft* computes the fast fourier transform values of the dataset $x[n]$. The fourier spectra was than plotted, and certain frequencies were filtered out.

7.4.2 Trigonometric Fourier series

The rotational measurements of H_{res} gives a periodic form. In order to identify the different contributions to H_{res}, it was expressed as a trigonometric Fourier series

$$H_{\text{res}} = H_0 - \sum_{n=1}^{(N+1)/2} H_n \cos(nx + \phi_n) \tag{7.3}$$

where

$$\begin{aligned} H_0 &= \frac{Y(1)}{L} \\ a_n &= \frac{2}{L} * \text{Re}\{Y(n+1)\} \\ b_n &= -\frac{2}{L} * \text{Im}\{Y(n+1)\} \\ H_n &= \sqrt{a_n^2 + b_n^2} \\ \phi_n &= \text{atan2}(b_n, a_n) - \pi \end{aligned} \tag{7.4}$$

and $Y = fft(H_{\text{res}})$ and the atan2 is the mathematical arctan-function which gives the correct value depending on the signs of a_n and b_n. The phase ϕ_n is shifted such that H_{res} can be written in the form of equation (3.20) This interpolation method was found by Gauss [54]. The form of H_{res} had significant contributions from the following terms:

$$H_{\text{res}}(x) \simeq H_0 - H_1 \cos(x - \phi_1) - H_2 \cos(2x - \phi_2) \tag{7.5}$$

Comparing equation (7.5) with equation (3.20): $x = \phi_H$, $H_0 = (\omega_0/\gamma)^2/4\pi M_{\text{eff}} - H_S$, $H_1 = H_E^{\text{FMR}}$ and $H_2 = H_K$. The phases ϕ_1 and ϕ_2 indicates the orientation of H_E^{FMR} and $H_2 = H_K$ to one another.

8 Thin films

Five different thin films were studied throughout this master project. 10Py/10Cu/4Cr/10Cu, 10Py/10Cu/7Cr/10Cu, 10Py/10Cu/10Cr/10Cu and 10Py/10Cu/13Cr/10Cu. The number in front of the material represents the thickness of the film in nanometers, while the slashes are interfaces between the materials. A sketch of the system is given in figure 8.1.

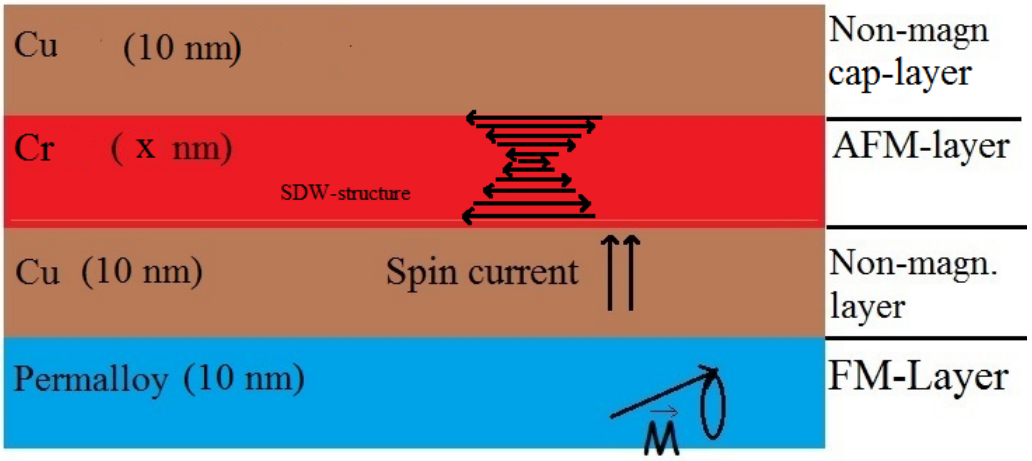

Figure 8.1: A sketch of the Py/Cu/Cr/Cu-system that was worked with. The precessing magnetization generating a spin current is illustrated in the permalloy and the copper-layer above it. The SDW-ordering of the spin is illustrated in the Cr-layer. However, this structure isn't necessarily the ordering or the SDW-amplitudes in the real system.

8.1 Permalloy (Py)

Permalloy is a nickel-iron magnetic alloy with about 20% iron and 80% nickel content. It possesses remarkable magnetic properties, such as a very high magnetic permeability at small field strengths [55]. Commercial permalloy typically have relative permeability of around 100000, compared to several 1000 for ordinary steel. Other magnetic properties include low coercivity, near zero magnetostriction and significant anisotropic magnetoresistance. The low magnetostriction makes it suitable for use in thin films for technological and industrial applications. The Curie temperature for Permalloy is $T_c = 853$ K [56],

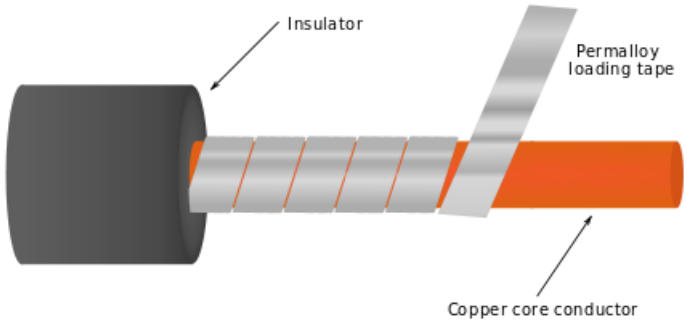

Figure 8.2: Example of an industrial application of permalloy. A submarine telegraph cable is wrapped with permalloy tape in order to reduce the distortion of the signal transmitted.

meaning that the magnetization as a function of temperature will follow the Bloch law, discussed in section 2.9.

8.2 Copper (Cu)

The major applications for copper are in electrical wires, roofing, plumbing and industrial machinery. However, in thin films, copper has an interesting property. In 2002 Mizukami *et. al* [57] conducted experiments (figure 8.3) with Cu/Py/Cu structures which showed a very slow increase in damping when the thickness of the last Cu-layer was increased.

This indicates that copper is a **good spin conductor**. One reason for this is the fact that the diffusion length of copper is very long ($\lambda_{sd} \sim 1\mu$m at low temperatures, and reduced to about 350 nm in room temperature [58]) compared to the film thickness considered in this project ($d_{Cu} = 10$nm). Copper conserves the polarization of the spin sink within λ_{sd}, and thus doesn't affect the Gilbert damping.

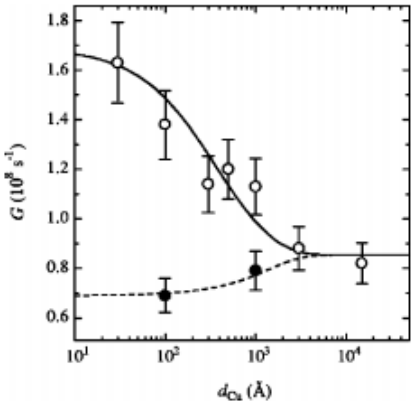

Figure 8.3: Gilbert damping constants (circles) measured in Cu/Py(3 nm)/Cu(d)/Pt films (white circles) and Cu/Py(3 nm)/Cu(d) (black circles) by Mizukami *et. al* [57] as a function of Cu-layer thickness d. Lines are the calculated data and are fitted with the experimental ones.

8.3 Chromium (Cr)

Chromium is remarkable due to its magnetic properties, as presented in section 4. Microscopicly, Cr is a bcc-structure with lattice constant $a = 2.884$ Å. Outside of technological applications, chromium is an important alloying material to steel. Stainless steel, the main corrosion-proof metal alloy, if formed when chromium is added to iron in sufficient concentrations, usually above 11 %.

Like other elements, chromium can oxidize when in contact with air. Chromium(VI)oxide (CrO_2) is the most common and stable form. CrO_2, like bulk Cr, is antiferromagnetic with T_N close to T_N of chromium 311 K. The chromium layer is subject to potential oxidation at temperatures above 300 K.

8.4 Thin film growth

The quality of the thin films depends on the deposition rate, ambient temperature, substrate temperature, pressure in the deposition chamber and cleaniness of the substrate surface [59]. As discussed in sections 2-4 the various film-properties are subject to the fabrication method. In addition, characterization methods are needed to identify the thicknesses and spin structure of each layer. This must be kept in mind when comparing

results with other work.

In this master work, the films were deposited on the same substrate, and in order. A deposition rate measurement was done before the film deposition. Since there was no way to monitor each deposition, the same deposition rate was assumed for each round of deposition. All other process parameters (appendix) were kept constant. Thickness characterization was not performed afterwards, meaning that an uncertainty in the thickesses must be assumed.

Several important magnetic properties are subject to uncertainties during the thin film growth. One property is the magnetocrystalline anisotripy constant in permalloy (2.6), K_U which gives rise to the anisotropy field H_2. Instead of sputtering 10 nm Py on a large substrate, and then sputtering Cu and Cr, the materials were sputtered in order inside the vacuum chamber. The reasoning for this was to ensure no impurities such as oxide or organic grains would grow on the materials when the substrate was removed from the deposition chamber. The anisotropy constant of Py is subject to internal stress in the material [7].

8.5 Cu and Cr interfaces

Growth of Cr on Cu(001) was investigated by Lawler *et al* [60] in 1996. They found the growth to be three dimensional in character with the formation of irregular multilayer islands forming four equivalent domains. The growth was in the temperature range 285-575 K and yielded that the deposited chromium became more bulk-like with increasing deposition temperature. Rouyer *et al* [61] found that Cr retains its bulk bcc structure when 6-30 monolayers of Cr are deposited on Cu(100).

Another aspect which is relevant to this work is what happens with the spin current from the Py-layer at the Cu/Cr-interface (figure 8.1). There are several effects discussed in section 5 and in the review article by [44], all of which can contribute to the various terms in the resonance field position (equation (3.20)). Examples of effects include reaction torques at the Cu/Cr-interface and diffusion inside the Cr layer. An extensive theoretical review of these topics has not been performed in this master work, but the potential effects must be taken into account before any conclusions are drawn.

8.6 Py and Cu interfaces

In addition to being a good spin conductor, copper serves as an oxide-protective layer of the permalloy film. In an FMR experiment, a small contribution to the exchange bias field is expected due to the Py/Cu having an interfacial coupling energy with an exchange coupling constant J_E. This is called the *Néel orange peel coupling* [62], and depends on the thickness of the non-magnetic layer. Kools *et al* [63] found that the exchange coupling constant J_E oscillates and decays with $1/t_{Cu}^2$, thus giving a contribution to $E_{\text{interface}}$ (equation (2.8)).

8.7 Chromium thin film properties with thicknesses 4, 7, 10 and 13 nm

A presentation of the magnetic properties of chromium in thin films was given in section 4.6. In order to analyse the FMR-results, the properties for each film thickness must be established. The two key properties are the SDW amplitude g, and the magnetic coupling constant J_{Coup}. Both parameters contribute to the interfacial exchange energy (section 2.7), which contributes to the resonance field position H_{res} (section 3.4). Based on the

theory presented in the sections above, an estimate of the contributions of each thickness will be given.

Recalling equation (2.8), the interfacial exchange energy is a sum of antiferromagnetic volume energy and interfacial coupling constant. This equation is valid for a ferromagnetic/antiferromagnetic bi-layer. Since chromium has a SDW structure, we can replace E_{VolAFM} with E_{SDW}. E_{SDW}, which was derived by Shi and Fishman [39], contains the exchange coupling constant J_E. Since there is a 10 nm thick Cu-layer in between the permalloy and chromium layers, there will be a reduction in the interfacial exchange energy term (equation (2.8)), which is valid for ferromagnetic and antiferromagnetic layers in direct contact. However, $E_{\text{interface}}$ increase when we take into account the spin pumping from the permalloy layer, which Brataas *et al* [44] showed gave an increase in the resonant field position, and thereby gives a contribution to the total energy term (equation 3.17).

Based on the theoretical studies in this work, along with the arguments/assumptions above, the discussion of the experimental results in this work will assume that $E_{\text{interface}} \propto g^2$, where g will follow Shi and Fishman's [39] model for the calculated values given in figure 4.15. The relevant properties of Cr are summarized in table 8.1.

Thickness (nm)	**Monolayers (ML)**	g	g^2
4	14	1.25	1.56
7	24	1.0	1.0
10	35	0.9	0.81
13	45	0.75	0.56

Table 8.1: Values of the SDW amplitude for each Cr thickness.

9 Experimental results and analysis

9.1 Overview

9.1.1 Experimental procedure

Experiments with the five thin films presented in section 8 was conducted. Small 1x1 mm samples of the film was carved using the scriber machine at NTNU Nanolab. The sample was placed in a quartz rod which was inserted into the resonant cavity. Table 1.2 shows the instrumental parameters used for the experiments. The parameters were chosen such that the resonance profile became as symmetric, high resolution and noise-free as possible. Each measurement took ∼1 hour.

The sample-temperatures ranged from 180 to 360 Kelvin, with the LN_2 heat power at 1% at the middle and higher temperatures and 4% at the lower temperatures. For each experiment, the sample was cooled down to and stabilized for a few minutes at 180 K. After the sweep was completed, the sample was heated and stabilized to 210 K with the external field switched off. This procedure continued for each ascending temperature up to 360 K. The sample was then cooled down to 295 K, the temperature the final sweep was conducted (this wasn't done on every sample).

9.1.2 How the data was processed

All the data was processed using the MATLAB script [64] created by Åsmund Monsen in 2013. The scripts were created using the EasySpin MATLAB package. Along with plotting the raw data, the script could fit the data with the Dysonian line-shape presented in section 7.3 and extract various key parameters described in sections 2, 3 and 7.3.

Various MATLAB scripts was then created by the author (Appendix) in order to analyse the data and show the important parameters.

9.2 Resonance field position and width of all samples

9.2.1 Opening remarks

One or two plots from each Cr-sample (4Cr denoting the 10Py/10Cu/4Cr/10Cu-sample, 7Cr denoting the 10Py/10Cu/7Cr/10Cu-sample, etc.) is presented. Figures 9.1(a)-9.4(a) show the resonance field position as a function of angle orientation at temperatures 180K, 210K, 240K, 280K and 330K. The legend box in each plot denotes the temperature of the sample, as well as the resonance field position at the first data point (0 degrees). Each graph is subtracted by the value of each of the respective values at 0 degrees. The legend box also shows the order the experiments were performed in.

Figures 9.1(b)-9.2(b) show the resonance field position as a function of angle orientation for various temperatures ranging from 280K to 360K. The legend box in each plot denotes the temperature of the sample, as well as the resonance field position at the first data point (0 degrees). Each graph is subtracted by the value of each of the respective values at 0 degrees. The legend box also shows the order the experiments were performed in. Due to similar behaviour in the 10Cr and 13 Cr at and above 330K, only the temperatures between 180-330K are shown.

Figures 9.5(a),(b) and 9.6 show the resonance width raw data for the 4Cr and 7Cr samples. The 10 Cr and 13 Cr-samples show a very noisy behaviour, very much like 7 Cr (figure 9.6). The 4 Cr shows a clear harmonic behaviour up to 330 K.

Only a few general observations will be discussed regarding the raw data. A more thorough discussion, as well as a presentation and comparison with the PyCu-sample will be given in section 9.3.

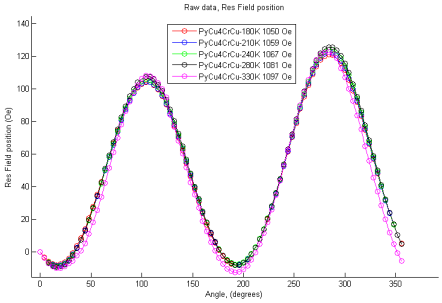

(a) Resonance field position as a function of sample orientation for the 10Py/10Cu/4Cr/10Cu-sample at temperatures 180K, 210K, 240K, 280K and 330K. The plots are shifted down by the value of the first data point (resonance field position at 0 degrees).

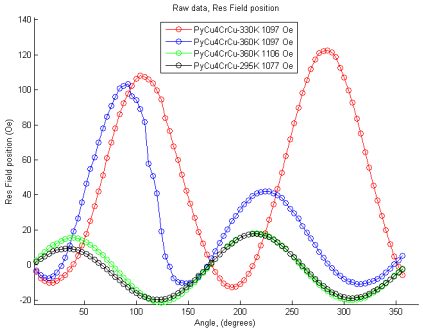

(b) Resonance field position as a function of sample orientation for the 10Py/10Cu/4Cr/10Cu-sample at temperatures 330K, 360K (trial 1), 360K (trial 2) and 295K. The plots are shifted down by the value of the first data point (resonance field position at 0 degrees).

Figure 9.1: 4Cr Resonance field position-overview

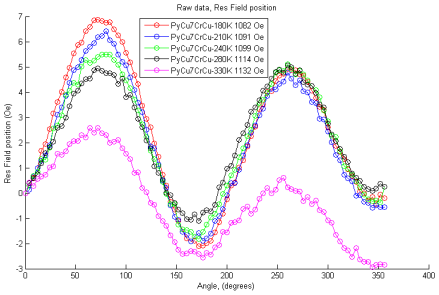

(a) Resonance field position as a function of sample orientation for the 10Py/10Cu/7Cr/10Cu-sample at temperatures 180K, 210K, 240K, 280K and 330K. The plots are shifted down by the value of the first data point (resonance field position at the 0 degree orientation).

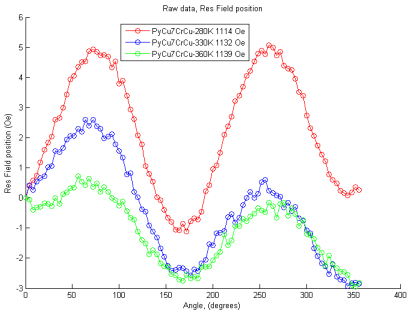

(b) Resonance field position as a function of sample orientation for the 10Py/10Cu/7Cr/10Cu-sample at temperatures 280K, 330K and 360K. Contrary to the other samples, a sweep at 295 K was not performed. The plots are shifted down by the value of the first data point (resonance field position at the 0 degree orientation).

Figure 9.2: 7Cr Resonance field position-overview

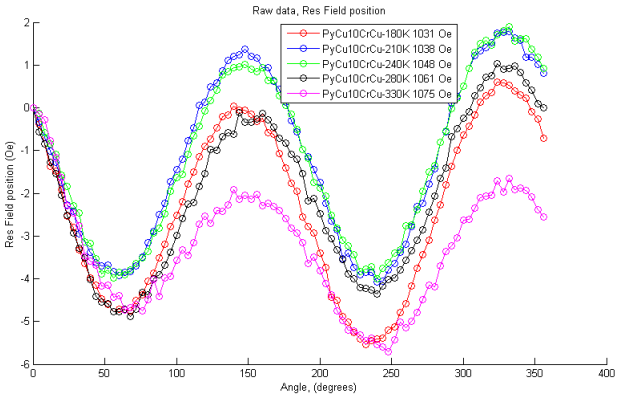

(a) Resonance field position as a function of sample orientation for the 10Py/10Cu/10Cr/10Cu-sample at temperatures 180K, 210K, 240K, 280K and 330K. The plots are shifted down by the value of the first data point (resonance field position at the 0 degree orientation).

Figure 9.3: 10Cr Resonance field position-overview

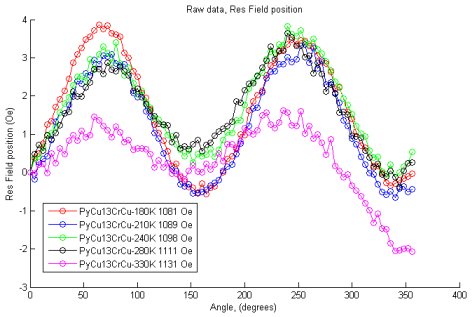

(a) Resonance field position as a function of sample orientation for the 10Py/10Cu/13Cr/10Cu-sample at temperatures 180K, 210K, 240K, 280K and 330K. The plots are shifted down by the value of the first data point (resonance field position at the 0 degree orientation).

Figure 9.4: 13Cr Resonance field position-overview

9.2.2 Discussion regarding the Resonance field raw data results

When inspecting the raw data, there are several interesting observations. First of all, the resonance field position is harmonic for all samples at temperatures up to 280K. It is also harmonic for the 4Cr sample at 330 K (figure 9.1(a)). However, for the 7Cr, 10Cr and 13Cr samples at 330K, as well as all four samples at 360K, the harmonic structure breaks down. We see that by observing that the endpoint (at 356°) does not approach the field position at the starting point (at 0°). This indicates a breakdown in the thin-film structure. When subsequent measurements at room temperature was conducted, a reproduction of the resonance profile (with the same amplitude at $\sim$ 280 K) was not seen.

The thin film samples are sensible to oxidation, especially above room temperature. The extent and exacly how the magnetic structure gets altered is unknown. It can be seen from figure 9.1(b) that the resonance peaks for the 4Cr-sample go from $\sim$100 Oe all the way down to $\sim$20 Oe, at the final room temperature measurement. Since the large amplitudes at the lower temperatures aren't reproducible after the sample has been above 300 K, we can say that the sample very likely has been oxidized.

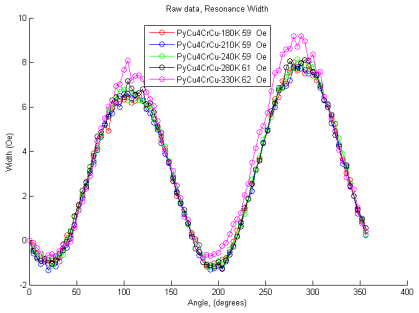

(a) Resonance width as a function of sample orientation for the 10Py/10Cu/4Cr/10Cu-sample at temperatures 180K, 210K, 240K, 280K and 330K. The plots are shifted down by the value of the first data point (resonance field position at 0 degrees).

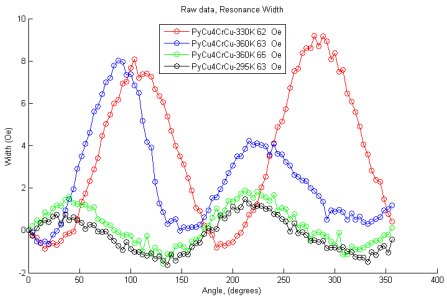

(b) Resonance width as a function of sample orientation for the 10Py/10Cu/4Cr/10Cu-sample at temperatures 330K, 360K (trial 1), 360K (trial 2) and 295K. The plots are shifted down by the value of the first data point (resonance field position at 0 degrees).

Figure 9.5: 4Cr Resonance width-overview

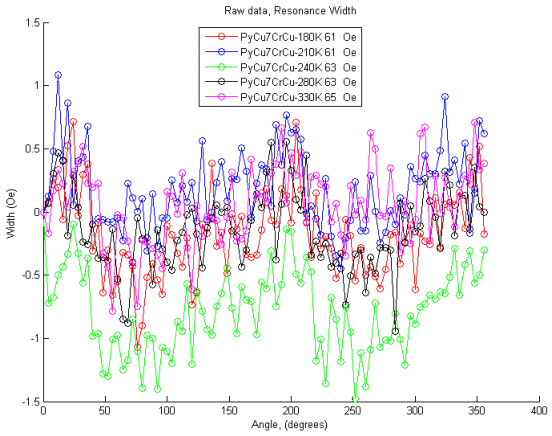

Figure 9.6: Resonance width as a function of sample orientation for the 10Py/10Cu/7Cr/10Cu-sample at temperatures 180K, 210K, 240K, 280K and 330K. The plots are shifted down by the value of the first data point (resonance width at the 0 degree orientation).

9.2.3 Discussion regarding the resonance width results

There is a clear harmonic structure in the 4 Cr sample with an amplitude of ∼4 Oe. It appears to be a small difference between the two maximum peaks of the width profile. At temperatures above 300K (figure 9.5(b)), there is also a breakdown similar to the resonance field profile (figure 9.1(b)). The form of equation (3.23), which describes a Py-thin film, gives a fair description of the resonance width profile. However, closely inspecting the raw data, a term $\propto \sin(\theta_h)$ gives a contribution to ΔH. For the 4 Cr film, it appears to be a contribution from the anisotropy field H_K. But to which extent is unknown, since it the various important mechanisms contributing to the resonance width has not been identified. As discussed in sections 5 and 8.5, contributions to the resonance width will come from spin pumping.

As for the 7 Cr sample (figure 9.6), the data isn't quite as good as the 4 Cr sample, but it appears to have a harmonic profile with two maximum peaks and an amplutide of ∼0.5 Oe. The plots of the 10 Cr and 13 Cr aren't included, but the data is distorted like the 7 Cr sample. The distortion also hides the predicted harmonic profile from the theoretical equation (3.23).

9.3 Results from Fourier interpolation

9.3.1 Opening remarks

The raw data of H_{res} from each sample was written in the form of equation (7.5). The field contributions H_0, H_1, H_2 and the phases ϕ_1, ϕ_2 for each sample, including PyCu at each temperature are plotted.

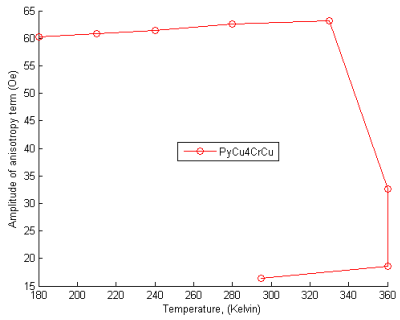

(a) H_2 for 4 Cr

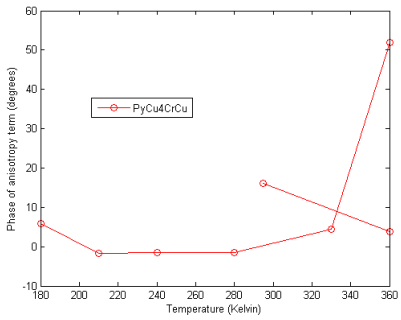

(b) ϕ_2 for 4 Cr

Figure 9.7: Anisotropy amplitude H_2 and phase ϕ_2 at the temperatures 180, 210, 240, 280, 330, 360 (2 trials) and 295K for 4 Cr

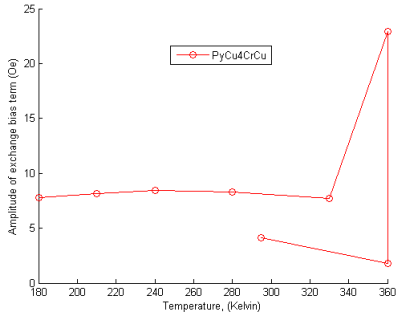

(a) H_1 for 4 Cr

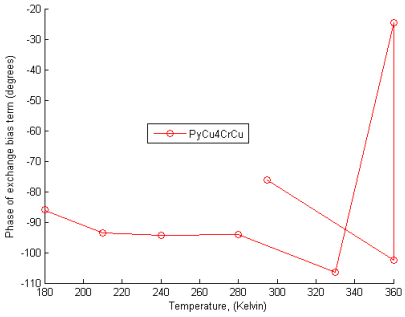

(b) ϕ_1 for 4 Cr

Figure 9.8: Exchange bias amplitude H_1 and phase ϕ_1 at the temperatures 180, 210, 240, 280, 330, 360 (2 trials) and 295K for 4 Cr

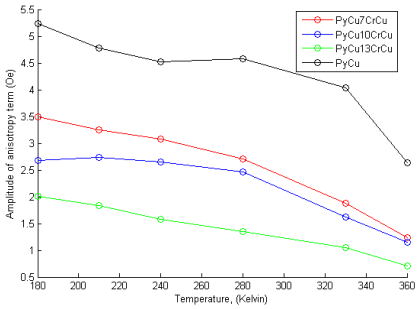

(a) H_2 for 7Cr, 10Cr, 13Cr and PyCu.

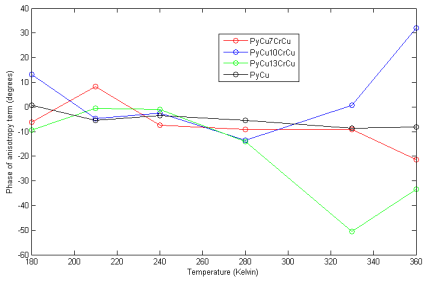

(b) ϕ_2 for 7Cr, 10Cr, 13Cr and PyCu.

Figure 9.9: Anisotropy amplitude H_2 and phase ϕ_2 at the temperatures 180, 210, 240, 280, 330 and 360K for 7Cr, 10Cr, 13Cr and PyCu.

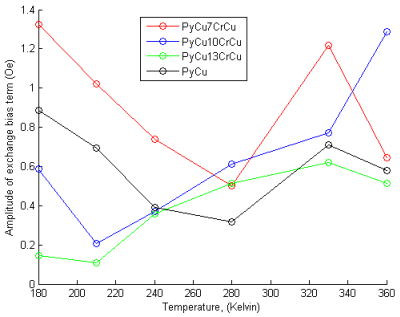

(a) H_1 for 7Cr, 10Cr, 13Cr and PyCu.

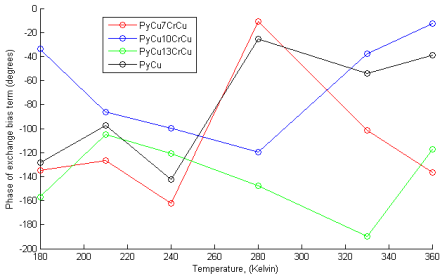

(b) ϕ_1 for 7Cr, 10Cr, 13Cr and PyCu.

Figure 9.10: Exchange bias amplitude H_1 and phase ϕ_1 at the temperatures 180, 210, 240, 280, 330 and 360K for 7Cr, 10Cr, 13Cr and PyCu.

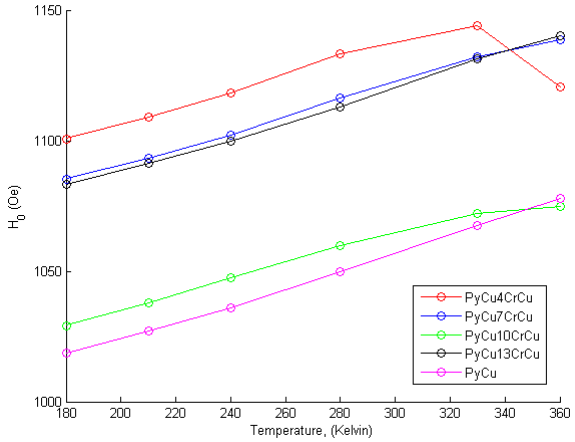

Figure 9.11: The offset field H_0 for all 5 samples at temperatures 180, 210, 240, 280, 330 and 360K.

9.3.2 Discussion regarding the offsett field H_0, the FMR exchange bias field H_1 and the anistropy field H_2 and their phases

As observed from the raw data plots of the resonance field (section 9.2), the 4Cr has a much higher anisotropy and exchange bias amplitude compared to the other three samples. Under 300K, the H_2 of 4Cr is $\sim$60 Oe which is about 30 times larger than H_2 of the other samples. The exchange bias amplitude H_1 for 4Cr is $\sim$8 Oe, which is about 10 times larger than H_1 of the other samples.

The phase ϕ_2 of the anisotropy term H_2 is relativly stable around 0° (with $\pm 10°$ fluctuation) for all samples at the temperatures 180-280K. The fluctuation is partly due to scaling of the raw data, in which the minimum of the resonance field position was set to start at 0°. The phase of the exchange bias term ϕ_1 hovers around $-90°$ for all samples at the temperatures 180-280K. The 4 Cr sample is more stable at $\phi_1 = -90°$ than the others.

Exchange bias The 7Cr, 10Cr and 13Cr samples revealed a very weak exchange bias field, indicating a weak exchange interface coupling with the permalloy layer. The exchange bias measured in the PyCu sample had comparable magnitude with the Cr-samples. This indicates a very weak exchange between the Py and Cr-layers. The exchange bias contribution from the PyCu sample comes from exchange coupling between the Py and Cu layer, including the Néel orange peel coupling (section 8.6) and internal defects of the Py layer. The exchange bias of each sample is very small in magnitude, $\sim 0.1 - 1.4$ Oe. Between the Py and Cr-layer, the SDW amplitude g (and thereby exchange bias H_1 is expected to decay with increasing Cr-thickness (section 8.7). The experimental results does not show a weaker H_1 with each thickness (with an exception of the 180 and 210K measurements), indicating that the SDW amplitude g gives a very small contribution, comparable with exchange coupling between Py/Cu to the exchange bias. We are unable to distinguish between these small effects. The ϕ_1-plot also confirms this. The very large fluctuations around $\phi_1 = -90°$ is due to various contributions to H_1 pointing at different directions.

The 4 Cr sample however, has an almost constant exchange bias $H_E \sim 8$ Oe and a more stable phase around $\phi_1 = -90°$ between 180K and 330 K. This indicates a stronger exchange coupling between the Py and Cr layer. This supports Shi and Fishman's [39] theory that a thinner Cr-film gives a larger SDW amplitude g, and thereby stronger contribution to H_1.

Anisotropy field The results for the anisotropy field H_2 show that it decreases for thicker Cr-layers. The anisotropy field also shows a small decrease with higher temperature for the 7Cr, 10Cr, 13Cr and PyCu samples. This decrease is expected due the uniaxial anisotropy constant decreasing with higher temperatures towards T_C (section 2.6). A major decrease in H_2 is not seen since the temperatures are well below $T_C = 853$K. The anistropy field of PyCu lies ~ 2 Oe above the 7 Cr sample. Similar to the exchange bias, the 4 Cr sample also has a much larger magnitude of H_2 than the other samples.

Offset field In the model used in this work, the offset field H_0 is a sum of a term involving the effective magnetization M_{eff} of the Py-layer and a term H_S coming from the spin pumping. Spin pumping takes place in each sample since we have a non-magnetic film on top of a ferromagnetic film (section 5). The higher resonance field in the Cr-samples can be explained in terms of a backflow of spin current from the Py-layer, into Cu, and reflected back at the Cu/Cr-interface and into the Py-layer again. Howerver, in the theoretical framework of this work, no conclusions can be drawn with this argument since the mechanisms at each interface is unknown.

It is also interesting to note that resonance field position decreases with higher thickness, with the exception of the 13 Cr-film, whose curve lies at a higher fields than the 10 Cr-film.

9.3.3 Difference between interpolated and raw data at each maximum

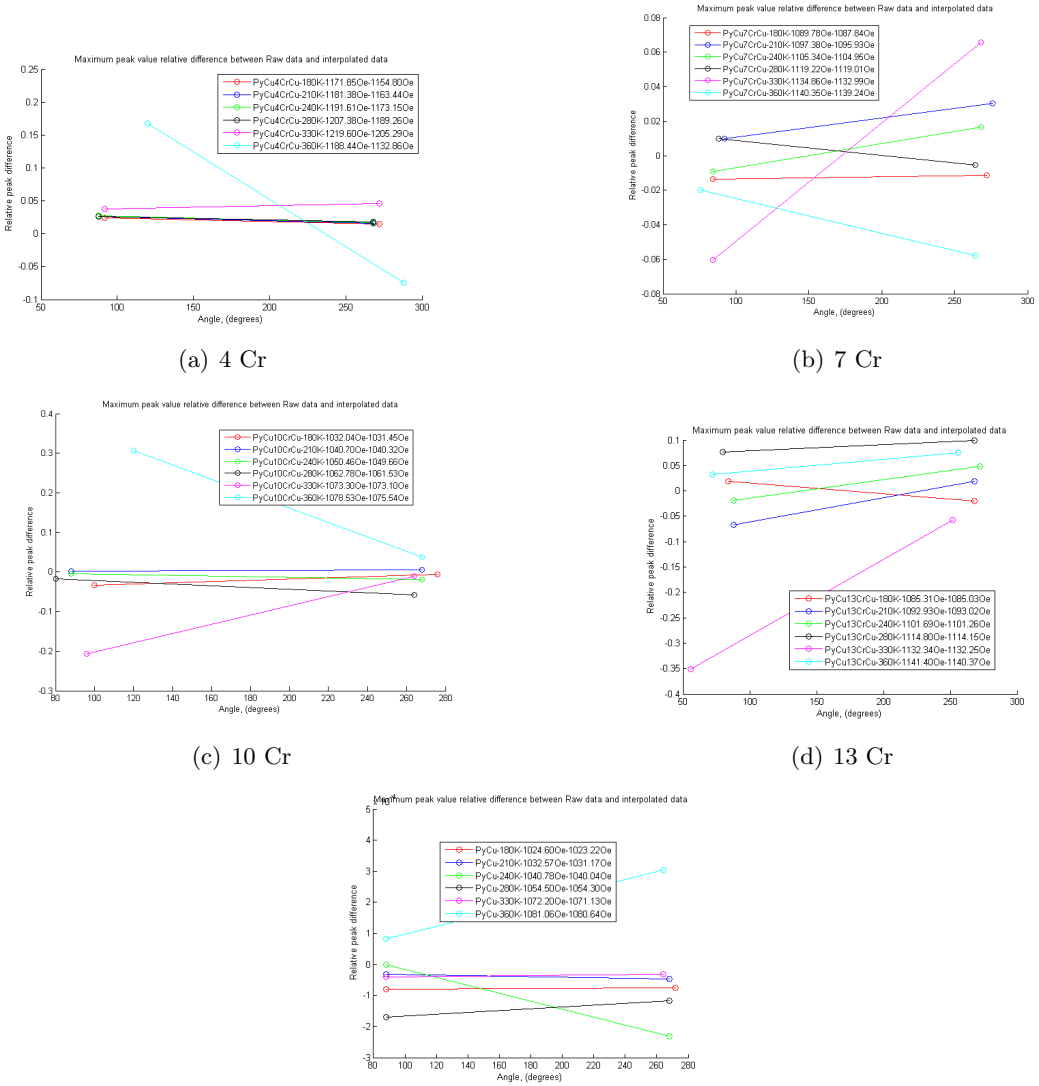

(a) 4 Cr

(b) 7 Cr

(c) 10 Cr

(d) 13 Cr

(e) PyCu

Figure 9.12: Difference in max-peaks between raw and interpolated data for all 5 samples at the temperatures 180, 210, 240, 280, 330 and 360K.

Remarks The relative peak difference between the raw data and the interpolated data at each maximum was calculated

$$r = \frac{H_{\text{RawData}}(\theta_{\text{Max}-1,2}) - H_{\text{Interpolated}}(\theta_{\text{Max}-1,2})}{H_{\text{RawData}}(\theta_{\text{Max}-1,2})} \tag{9.1}$$

and plotted in figures 9.12(a)-(e). Below 300 K for the PyCu, 4Cr, 7Cr and 10 Cr sample, the absolute value of the relative error is witin 5% indicating that the Fourier interpolation is a good fit. However, for the 13 Cr sample, the error is up to 10%. Both experimental (systematic errors discussed later) and data analysis-errors are sources for this. For instance, the the peaks should theoretically be located at $\theta = 90°, 270°$ since the data was shifted such that the minimum of H_{Res} started at $\theta = 0°$. This wasn't the case for all

measurements. As can be seen at the raw data, the tops aren't easy to identify for all the samples.

9.4 Average resonance width as a function of temperature

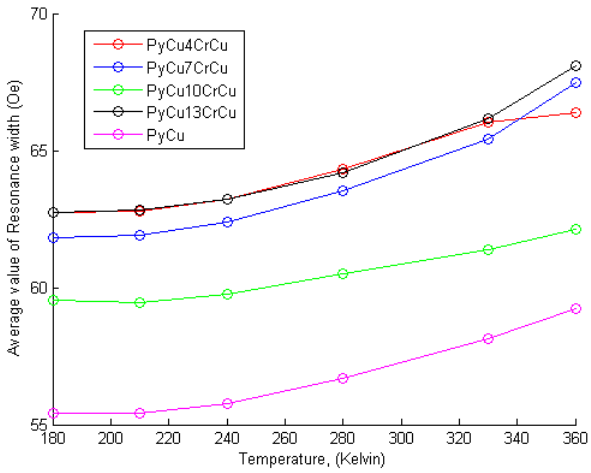

Figure 9.13: Average resonance width of all samples at temperatures 180, 210, 240, 280, 330 and 360K.

9.4.1 Discussion regarding the average width.

In section 3.6 experimental results revealed an approximately constant ΔH for $T = 180 - 300$K. The experimental results in this work show that this is almost the case, but we do see a small increase which grows at the higher temperature. The samples with Cr have a higher resonance width than PyCu. This is partly due to spin pumping, which enhances the damping (section 5.5). Also, interfacial effects at the Cu/Cr-layer discussed in section 8.5 may contribute to the increased resonance width compared to the PyCu-sample. There is spin pumping in the PyCu sample, but how much this contributes to the resonance width is not known, since we haven't measured a Py-reference sample.

9.4.2 Resonance field position as a function of temperature

Inspecting figure 9.14, it can be seen that H_0 follows the Bloch $T^{3/2}$ presented in section 3.5. Another interesting observation is the thickness dependence. It can be seen that H_0 decreases with increasing thickness, with the exception of the 13 Cr sample. The 13 Cr curve lies very close with the 7 Cr curve, but at a higher H_0 than 10 Cr. PyCu has a lower H_0 than the Cr-samples (up to 330 K).

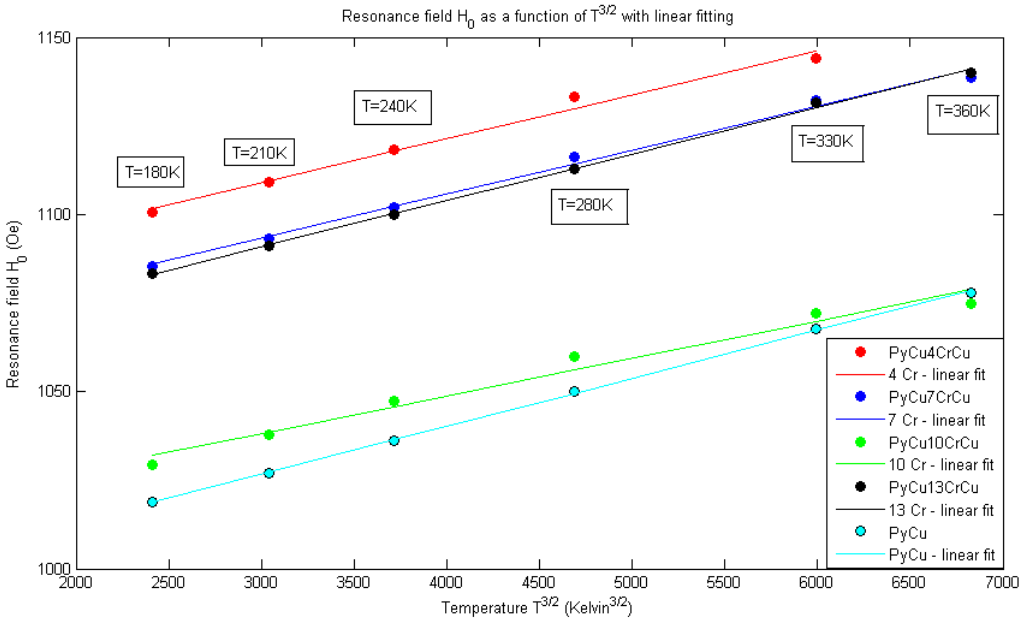

Figure 9.14: T32 linfit.

9.5 General discussion

A comprehensive discussion of all the results will be presented in the following section. A summary of what this work has accomplished in gaining knowledge of a spin-pumping FM/NM/AFM/NM will be given. Hypothesis which were set before the experimental work and theoretical study, which later proved to be wrong will also be given.

9.5.1 Néel transition

The Néel temperature of Chromium is 311 K, which is in the temperature range studied in this work. When the antiferromagnetic phase transforms into a paramagnetic phase, the interface coupling with permalloy disappears. Thus the exchange bias H_E is zero. This was not the case for any of the 4 chromium sample, implying that the chromium layer keeps its antiferromagnetic state at temperatures above T_N. This result confirms theory from Shi and Fishman [39] who found that chromium has a T_N over the bulk value (313 K) in thin films. In order to control the exchange bias in the film, field cooling through T_N must be done on the film (section 4.2). In the case of the chromium films, T_N must be found with a capping layer that can withstand the high temperature.

9.5.2 Applicability of the equations for H_{Res} and E_{Tot}

The equations (3.18) and (3.20) are based on the model by Yuan [18] for a ferromagnetic/antiferromagnetic thin film multilayer. When looking at the experimental results for H_{Res}, the form of equation (7.5) is a good fit. However, more theoretical studies is needed in order to identify which energies give a significant contribution to the resonance field position. Since the raw data was fitted quite well, the experimental results for H_0, H_1, H_2 will serve as a good reference for future work.

9.5.3 Applicability of the equations for ΔH

The theoretical formula for ΔH (equation (3.23)) used in this work is for a single Py-film. Due to many factors contributing to the resonance width, it is difficult to extract any properties using this model. Since we see a clear profile for the 4 Cr-sample a model can be adapted. This is not the case for the 7Cr - 13Cr samples, which need to be measured (if possible) in higher resolution so a (if possible) harmonic profile can appear.

9.5.4 4Cr vs. 7Cr, 10 Cr and 13 Cr-systems

The 4Cr film had vastly higher anisotropy and exchange bias than the other Cr-films. However, the offset field H_0 and average line width ΔH are of the same magnitude as the other films. In the theoretical framework of this master thesis, only one explanation can be given: The 4 Cr-film has the highest SDW amplitude g (section 8.7) which increases the exchange bias H_E. The higher magnitude in the anisotropy field H_K, which in the theoretical model in this worked, is assumed to be proportional with the in-plane uniaxial anistropy constant K_U in Py. The presence of the 4 Cr film might be the reason for an enhancement of K_U. But it may also enhance other parameters which are proportional H_K that hasn't been considered in this work. The offset field H_0 for 4 Cr lies $\sim$ 10Oe higher than the 7 Cr-film. The relatively small differences between 4 Cr and the other samples in H_0 and ΔH can't be explained within the theoretical framework.

9.5.5 Temperature effects

The temperature measurements of H_0 and ΔH both follow theoretical and experimental studies based on permalloy/iron thin films from other works (section 3.5 and 3.7). Since the resonance field position follows the Bloch $T^{3/2}$, we can argue that $M(T)$ of the system also follows Bloch's $T^{3/2}$ law (equation (2.11)), which is valid at temperatures sufficiently below T_C. This indicates that the presence of Cr doesn't alter the magnetization in permalloy.

9.5.6 Deviations due to systematic errors during thin-film growth

The 5 thin films investigated in this work was attempted to be fabricated and optimized in the best possible way given the tools available. The ideal system would be to have:

- Perfect interfaces between the layers, meaning no alloying.
- Equal permalloy layers in each sample, with the same amount of defects.
- No oxidation between the fabrication and the FMR experiment.
- Perfect vacuum during deposition, meaning no air or dust particles in the material system.

- A clean Si-wafer with no air, dust or organic materials.

A pre-study of these factors was conducted. Several samples were also created and studied. Unsatisfactory results led to further optimizing the system, until the set of 5 thin films used in this work was created. During the early stages, there was problems with the sputter-instrument mainly due to unstable plasma. The plasma needs to be kept stable and equal for all thin films. This was not achieved until the final round of deposition. By checking the parameters (refer to appendix) at the control screen and ensuring they were stable, the deposition was optimized. However there was no way to monitor the deposition microscopicly. The wafers were etched in an oxygen plasma for 1 minute (a standard amount of time) before deposition, hopefully leading to satisfactory cleaning of the surface.

During deposition there are a few potential systematic errors. Firstly, the shutters for the target materials need to be shut properly after the desired thickness of the material is reached. The shutters on each target material were not perfect, and some material may have reached the substrate after the deposition was completed. The time between each layer which was deposited was between 3-5 minutes, which hopefully is enough time to remove any excess material from the previous material out of the vacuum chamber. Regardless, the same method and parameters were repeated for all 5 samples.

9.5.7 Deviations due to systematic errors during FMR-experiment

The anisotropy field H_2 is proportional to the uniaxial anisotropy constant of Py, K_U (equation (3.20). K_U depends on the crystal structure, grain orientations and internal stresses of the material. As previously discussed, mapping this out microscopicly was not possible. This means that deviations of K_U in each sample might be expected.

During the FMR-experiment a couple of potential error sources must be considered. At first, the incrementation of the angle orientation ϕ, which is controlled by the instrument. A small deviation in the orientation might occur if the sample unexpectedly moves inside the cavity. The second is the sample temperature. A deviation between the temperature measured by a sensor inside the cavity and the actual sample temperature might be expected. In order to ensure the most accurate sample temperature as possible, the sample rested at the target temperature for 5 minutes before the FMR measurement was performed.

10 Conclusion

A theroretical and experimental study of 10Py/10Cu, 10Py/10Cu/xCr/10Cu (with x=4,7, 10,13 nm) thin films has been performed. The thin films were fabricated at NTNU Nanolab and afterwards a FMR-experiment were performed on them at the temperatures 180K, 210K, 240K, 280K, 330K and 360K. The raw data was fitted to a Dysonian lineshape, and the resonance field position H_{Res} and resonance width ΔH was stored as a function of angle. H_{Res} was then Fourier interpolated in order to distinguish the different contributions: Anisotropy field, exchange bias, offset field, and their phases.

The results revealed vastly higher magnitude of anisotropy field and exchange bias for the 4 Cr film, compared to the other samples. Under 300K, the anisotropy field of 4Cr is $\sim$60 Oe which is about 30 times larger than anisotropy field of the other samples. The exchange bias for 4Cr is $\sim$8 Oe, which is about 10 times larger than the exchange bias of the other samples. The significant difference in exchange bias is explained by the spin-density wave amplitude, which increases for decreasing Cr-thicknesses. However, this model does not predict the large drop-off to the 7 Cr, 10 Cr and 13 Cr samples. The measurement of PyCu revealed an exchange bias of the same order as the 7-13 Cr samples, indicating that the exchange coupling between the Py and Cr layer is very weak, since it is of the same magnitude as the PyCu film.

No sign of a phase transition for Cr at the Néel temperature 311 K was found. A theoretical study revealed that the Néel temperature increased with decreasing Cr-thickness. In addition, measurements above 300 K gave erratic results which is concluded to be due to oxidation of the Cu and Cr-layer.

A theoretical description of H_{Res} and ΔH of the system was given, but not fulfilled. Factors, mainly due to spin pumping and interface effects must be identified and adapted to the equations.

11 Future prospects

This master work, along with the preceding project work has helped gain more insight on FM/NM/AFM/NM-systems. There is a strong anisotropy and exchange bias in the 4 Cr-sample. More work needs to be done in order to understand why this is the case.

One aspect which can be studied is setting the direction of the exchange bias with field cooling. In order to do this, one needs to find T_N for the 4 Cr, and have a sufficient capping layer which can withstand oxidation above room temperature. Setting the exchange bias is important in technological applications.

The only experimental setup in this master work was the EPR-spectrometer. Several other experiments can be performed in order to map out other interesting properties, such as the magnetization curve and anisotropy constants. The spin transport-properties of the system can also be mapped out experimentally. One can also find ways to monitor the film growth process.

A reference 10Py sample can also be analysed and compared with the other samples. It is interesting to know how the fields H_0, H_1, and H_2, are relative to the other samples. More conclusions can be drawn when the properties are known. Higher thicknesses of Cr is also of interest in order to draw more definitive conclusions in regards to thickness dependence.

Bibliography

[1] Johannes Ofstad. Ferromagnetic Resonance Spectroscopy Studies of FM/N-M/AFM/NM Thin-Films, 2013.

[2] D.L Mills and J.A.C Bland. *Nanomagnetism: Ultrathin Films, Multilayers and Nanostructures.* Elsevier, 2006.

[3] W. H. Meiklejohn and C. P. Bean. New magnetic anisotropy. *Phys. Rev.*, 105:904–913, Feb 1957.

[4] D.J. Griffiths. *Introduction to electrodynamics.* Prentice Hall, 1999.

[5] A. Hubert and R. Schäfer. *Magnetic Domains: The Analysis of Magnetic Microstructures.* Springer, 1998.

[6] P. Bruno. Physical origins and theoretical models of magnetic anisotropy. *Magnetismus von Festkorpern und grenzflachen*, 24:1–28, 1993.

[7] B. D. Cullity and C. D. Graham. *Introduction to Magnetic Materials.* Wiley-IEEE Press, 2 edition, 2008.

[8] Haiwen Xi, Keith R. Mountfield, and Robert M. White. Ferromagnetic resonance studies of exchange biasing in ni81fe19/pt10mn90 bilayers. *Journal of Applied Physics*, 87(9), 2000.

[9] C. Kittel. *Introduction to Solid State Physics.* Wiley, 2005.

[10] Pierre Weiss and R Forrer. The atomic moments of iron cobalt and nickel as determined from the magnetic saturation of the ferro-cobalts and nickel-cobalts. *Proceedings of the Physical Society*, 42(5):413, 1930.

[11] Michael Farle. Ferromagnetic resonance of ultrathin metallic layers. *Reports on Progress in Physics*, 61(7):755, 1998.

[12] B. Heinrich and J. F. Cochran. Ultrathin metallic magnetic films: magnetic anisotropies and exchange interactions. *Adv. Phys.*, 42, 1993.

[13] Lev Davidovich Landau and E Lifshitz. On the theory of the dispersion of magnetic permeability in ferromagnetic bodies. *Phys. Z. Sowjet.*, 8:153, 1935.

[14] J.H.E Griffiths. Anomalous high-frequency resistance of ferromagnetic metals. *Nature*, 158:670–671, 1946.

[15] Charles Kittel. On the theory of ferromagnetic resonance absorption. *Phys. Rev.*, 73:155–161, Jan 1948.

[16] D. Polder. On the theory of ferromagnetic resonance. *Philosophical Magazine*, 40:99–115, 1949.

[17] H. Suhl. Ferromagnetic resonance in nickel ferrite between one and two kilomegacycles. *Phys. Rev.*, 97:555–557, Jan 1955.

[18] S. J. Yuan, Y. X. Sui, and S. M. Zhou. Isotropic ferromagnetic resonance field shift in as-prepared permalloy/femn bilayers. *The European Physical Journal B - Condensed Matter and Complex Systems*, 44(4):557–562, 2005.

[19] M. Diaz de Sihues, C.A. Durante-Rincon, and J.R. Fermin. A ferromagnetic resonance study of nife alloy thin films. *Journal of Magnetism and Magnetic Materials*, 316(2):e462 – e465, 2007. ¡ce:title¿Proceedings of the Joint European Magnetic Symposia¡/ce:title¿.

[20] B.K. Kuanr, V. Veerakumar, A.V. Kuanr, R.E. Camley, and Z. Celinski. Effect of temperature on the ferromagnetic-resonance field and line width of epitaxial fe thin films. *Magnetics, IEEE Transactions on*, 45(10):4015–4018, 2009.

[21] R. D Hempstead and S. Krongelb. Unidirectional anisotropy in nickel-iron films by exchange coupling with antiferromagnetic films. *Magnetics, IEEE Transactions on*, 14(5):521–523, 1978.

[22] J. M. Logan, H. C. Kim, D. Rosenmann, Z. Cai, R. Divan, O. G. Shpyrko, and E. D. Isaacs. Antiferromagnetic domain wall engineering in chromium films. *Applied Physics Letters*, 100(19):–, 2012.

[23] http://physics.unl.edu/tsymbal/reference/giant_magnetoresistance/gmr_structures.shtml.

[24] J. Belleson and E. Grochowski. The era of giant magnetoresistive heads. *Hitachi Global Storage Technologies*, 1998.

[25] http://www.promconversia.com/eng/magnet/gmr.

[26] L. M. Corliss, J. M. Hastings, and R. J. Weiss. Antiphase antiferromagnetic structure of chromium. *Phys. Rev. Lett.*, 3:211–212, Sep 1959.

[27] G.E. Bacon. A neutron-diffraction study of very pure chromium. *Journal Name: Acta Cryst.*, Aug 1961.

[28] G E Bacon and N Cowlam. Magnetic studies of annealed and alloyed chromium by neutron diffraction. *Journal of Physics C: Solid State Physics*, 2(2):238, 1969.

[29] P M Marcus, S-L Qiu, and V L Moruzzi. The mechanism of antiferromagnetism in chromium. *Journal of Physics: Condensed Matter*, 10(29):6541, 1998.

[30] S. Blügel, D. Pescia, and P. H. Dederichs. Ferromagnetism versus antiferromagnetism of the cr(001) surface. *Phys. Rev. B*, 39:1392–1394, Jan 1989.

[31] G. Grüner. The dynamics of spin-density waves. *Rev. Mod. Phys.*, 66:1–24, Jan 1994.

[32] A. W. Overhauser. Giant spin density waves. *Phys. Rev. Lett.*, 4:462–465, May 1960.

[33] A. W. Overhauser. Spin density waves in an electron gas. *Phys. Rev.*, 128:1437–1452, Nov 1962.

[34] Eric Fawcett. Spin-density-wave antiferromagnetism in chromium. *Rev. Mod. Phys.*, 60:209–283, Jan 1988.

[35] Z Barak and M B Walker. Theory of the magnetic phase diagram and torque for chromium near its spin-flip temperature. ii. *Journal of Physics F: Metal Physics*, 11(4):947, 1981.

[36] J. W. Allen and C. Y. Young. Magnetic anisotropy due to spin-orbit and dipole-dipole interactions in spin-density-wave antiferromagnets. *Phys. Rev. B*, 16:1103–1108, Aug 1977.

[37] P. Bödeker, A. Schreyer, Zabel, and H. Spin-density waves and reorientation effects in thin epitaxial cr films covered with ferromagnetic and paramagnetic layers. *Phys. Rev. B*, 59:9408–9431, Apr 1999.

[38] Kunitomo Hirai. Spin density wave in fecr superlattices: A first principles study. *Phys. Rev. B*, 1999.

[39] Zhu-Pei Shi and R. S. Fishman. Interplay between spin-density wave and proximity magnetic layers. *Phys. Rev. Lett.*, 78:1351–1354, Feb 1997.

[40] J. Unguris, R. J. Celotta, and D. T. Pierce. Magnetism in cr thin films on fe(100). *Phys. Rev. Lett.*, 69:1125–1128, Aug 1992.

[41] Mark Johnson and R. H. Silsbee. Interfacial charge-spin coupling: Injection and detection of spin magnetization in metals. *Phys. Rev. Lett.*, 55:1790–1793, Oct 1985.

[42] G. Binasch, P. Grünberg, F. Saurenbach, and W. Zinn. Enhanced magnetoresistance in layered magnetic structures with antiferromagnetic interlayer exchange. *Phys. Rev. B*, 39:4828–4830, Mar 1989.

[43] E.D Barco A.D Kent and B. Ozyilmaz. Spin-transfer-induced precessional magnetization reversal. *Applied Physics Letters*, 84:3897–3900, 2004.

[44] Yaroslav Tserkovnyak, Arne Brataas, Gerrit E.W. Bauer, and Bertrand I. Halperin. Nonlocal magnetization dynamics in ferromagnetic heterostructures. *Rev.Mod.Phys.*, 77:1375–1421, 2005.

[45] M. D. Stiles and A. Zangwill. Anatomy of spin-transfer torque. *Phys. Rev. B*, 66:014407, Jun 2002.

[46] K. Xia, P. J. Kelly, G. E. W. Bauer, A. Brataas, and I. Turek. Spin torques in ferromagnetic/normal-metal structures. *Phys. Rev. B*, 65:220401, May 2002.

[47] John E Mahan. Physical vapor deposition of thin films. *Physical Vapor Deposition of Thin Films, by John E. Mahan, pp. 336. ISBN 0-471-33001-9. Wiley-VCH, January 2000.*, 1, 2000.

[48] http://ntnu.norfab.no/webforms/equipment/equipmentview.aspx?toolid=73.

[49] http://www.ajaint.com/.

[50] http://www.bruker.com/en/products/mr/epr/elexsys/e500/overview.html.

[51] http://98.130.33.227/index.php?show=productsprodid=122.

[52] Freeman J. Dyson. Electron spin resonance absorption in metals. ii. theory of electron diffusion and the skin effect. *Phys. Rev.*, 98:349–359, Apr 1955.

[53] L. Chaparro. *Signals and Systems using MATLAB*. Elsevier Science, 2010.

[54] C. F. Gauss. Nachlass: Theoria interpolationis methodo nova tractata. In *Werke*, volume 3, pages 265–330. Königliche Gesellschaft der Wissenschaften, Göttingem, 1866.

[55] H. D. Arnold and G.W. Elmen. Permalloy, A New Magnetic Material of Very High Permeability. *Bell System Tech. J*, 2:101–111, 1923.

[56] R Ranchal, C Aroca, and E Lopez. Domain walls and exchange-interaction in permalloy/gd films. *New Journal of Physics*, 10(1):013013, 2008.

[57] S. Mizukami, Y. Ando, and T. Miyazaki. Effect of spin diffusion on gilbert damping for a very thin permalloy layer in cu/permalloy/cu/pt films. *Phys. Rev. B*, 66:104413, Sep 2002.

[58] A. T. Filip F. J. Jedema and B. J. van Wees. Electrical spin injection and accumulation at room temperature in an all-metal mesoscopic spin valve. *Nature*, 410:345–348, 2001.

[59] Kulkarni and Chang. Electrical and structural characteristics of chromium thin films deposited on glass and alumina substrates. *Thin Solid*, 1997.

[60] J. F. Lawler, R. G. P. van der Kraan, H. van Kempen, and A. J. Quinn. Growth of cr on cu(001) studied by scanning tunneling microscopy. *Phys. Rev. B*, 53:11159–11163, Apr 1996.

[61] MC. Hanf D. Bolmont D. Rouyer, C. Krembel and G. Gewinner. Epitaxy of thin cr layers on cu(001). *Surface Science*, 1994.

[62] B. D. Schrag, A. Anguelouch, S. Ingvarsson, Gang Xiao, Yu Lu, P. L. Trouilloud, A. Gupta, R. A. Wanner, W. J. Gallagher, P. M. Rice, and S. S. P. Parkin. Neel orange-peel coupling in magnetic tunneling junction devices. *Applied Physics Letters*, 77(15), 2000.

[63] J. C S Kools, Th G S M Rijks, A. E M De Veirman, and R. Coehoorn. On the ferromagnetic interlayer coupling in exchange-biased spin-valve multilayers. *Magnetics, IEEE Transactions on*, 31(6):3918–3920, 1995.

[64] Åsmund Monsen. Reader_v10_dysoninan_1peak.m.

1 Appendix

Sputter deposition parameters

Parameter/Material	**Value**
Argon pressure	3-5mTorr
Argon flow	67 sccm
Substrate temperature	Room temperature
Base vacuum	$5 \cdot 10^{-8}$ Torr
Permalloy	10 nm
Deposition rate	0.9 Å/s
Duration	109 s
Operating effect	293 W
Power source	RF
Copper	10 nm
Deposition rate	1.7 Å/s
Duration	58 s
Operating effect	178 W
Power source	DC
Chromium	4-13 nm
Deposition rate	0.8 Å/s
Duration	50-163 s
Operating effect	178 W
Power source	DC

Table 1.1: Instrument parameters used for the sputter deposition.

EPR Spectrometer parameters

Parameter	Value
Resonance frequency	∼9,59 GHz
Magnetic field range	600-2000 Gauss
Number of data points	1500
Attenuation gain	60 dB
Power	2 mW
Angle range	0-360°
Angle step	4°
Temperature tolerance	1°K
Heat power limit	30 %
LN_2 heat power	1-4 %
Receiver gain	40 dB
Time constant	10.24 ms
Conversion time	20.48 ms

Table 1.2: Parameters used on the EPR spectrometer 7.2. The frequency was fine tuned for each slice scan. Receiver gain, time constant and conversion time are all parameters for the detection.